2014

Layered mixing on the New England Shelf in summer

Wang, Jianing

Wang, J., B. J. W. Greenan, Y. Lu, N. S. Oakey, and W. J. Shaw (2014), Layered mixing on the
þÿNew England Shelf in summer, J. Geophys. Res. Oceans, 119, 5776 579

AGU PUBLICATIONS

JGR

Journal of Geophysical Research: Oceans

RESEARCH ARTICLE

10.1002/2014JC009947

Layered mixing on the New England Shelf in summer

Jianing Wang[1,2], Blair J. W. Greenan[3], Youyu Lu[3], Neil S. Oakey[3], and William J. Shaw[4]

[1]Key Laboratory of Ocean Circulation and Waves, Institute of Oceanology, Chinese Academy of Sciences, Qingdao, China, [2]Laboratory of Physical Oceanography, College of Physical and Environmental Oceanography, Ocean University of China, Qingdao, China, [3]Bedford Institute of Oceanography, Fisheries and Oceans of Canada, Dartmouth, Nova Scotia, Canada, [4]Oceanography Department, Naval Postgraduate School, Monterey, California, USA

Key Points:
- Layered structure of stratification on the New England Shelf
- Mixing characteristics of the ocean interior and bottom boundary layer
- Variation of mixing associated with stratification and tidal and subtidal flows

Correspondence to:
B. J. W. Greenan,
Blair.Greenan@dfo-mpo.gc.ca

Citation:
Wang, J., B. J. W. Greenan, Y. Lu, N. S. Oakey, and W. J. Shaw (2014), Layered mixing on the New England Shelf in summer, *J. Geophys. Res. Oceans*, *119*, 5776–5796, doi:10.1002/2014JC009947.

Received 7 MAR 2014
Accepted 3 AUG 2014
Accepted article online 7 AUG 2014
Published online 5 SEP 2014

Abstract The layered structure of stratification and mixing on the New England Shelf (NES) in summer is examined by analyzing a comprehensive set of observations of hydrography, currents and turbulence. A clear distinction in mixing characteristics between the midcolumn water (consisting of subsurface stratification, middepth weak stratification and lower-layer stratification) and a well-mixed bottom boundary layer (BBL) is revealed. The combination of subtidal Ekman onshore bottom transport and cross-shore density gradient created a lower-layer stratification that inhibited the upward extension of the BBL turbulence. The BBL mixing was related to strong shear generated by bottom stress, and the magnitude and periodic variation of BBL mixing was determined by both the tidal and subtidal flows. Mixing in the midcolumn water occurred under stably stratified conditions and showed correspondence with the occurrence of near-inertial and semidiurnal internal waves. Positive correlations between buoyancy frequency squared (N^2) and shear variance (S^2), S^2 and dissipation rate (ε), N^2 and ε are established in the midcolumn, but not in the BBL. The midcolumn ε was reasonably described by a slightly modified MacKinnon-Gregg (MG) model.

1. Introduction

Turbulent mixing in shelf seas plays a crucial role in determining circulation as well as the distribution of heat, salt, nutrients, sediments and pollutants [*Sharples et al*., 2001; *Carter et al*., 2005]. The structure of the shelf water column is governed by the balance between heating at surface and mixing generated by tidal flow and surface wind [*Simpson and Hunter*, 1974]. Previous studies examined regimes of mixing due to various processes and explored different parameterization schemes [e.g., *Simpson et al*., 1996; *Sundermeyer and Ledwell*, 2001; *MacKinnon and Gregg*, 2005b; *Burchard et al*., 2008; *Liu*, 2010; *Palmer et al*., 2013]. In the bottom boundary layer (BBL), turbulence is mainly attributed to velocity shear driven by bottom stress. *Inall et al*. [2000] and *Liu et al*. [2009] found that over half of the observed dissipation occurred in the BBL. Turbulence driven by bottom stress can significantly influence the structure of water column in shelf seas depending on the thickness of the BBL [*Simpson et al*., 1996; *Rippeth et al*., 2003; *Simpson and Tinker*, 2009]. Other processes such as surface waves in shallow water and internal waves can also represent sources of the BBL turbulence. For example, *Davis and Monismith* [2011] found that turbulence in the BBL over a barrier reef was highly variable in time and modified by shoaling internal waves. *Richards et al*. [2013] distinguished the contributions from tidal shear and shoaling internal waves to the BBL turbulence in an estuary, and found that the observed dissipation rate (ε) of turbulent kinetic energy (TKE) exceeded values associated with tidal shear by an order of magnitude during periods of high internal wave activity.

In the midcolumn layer away from the boundary, turbulence can also be induced by bottom shear stress as previously discussed, especially when stratification is weak. On the other hand, bottom-driven turbulence can be damped by stratification in which case internal waves may be the primary mechanism driving midcolumn mixing. This could be due to internal wave-driven instability, which depends on the gradient Richardson number similar to the bottom stress driven instability [e.g., *Rippeth* 2005; *Rippeth et al*., 2005; *Palmer et al*., 2013]. Alternatively, turbulence in stably stratified layers has been observed [*Palmer et al*., 2008, 2013] and different models have been proposed to scale the distributions of ε [*Henyey et al*., 1986; *Gregg*, 1989; *MacKinnon and Gregg*, 2003b, 2005b].

The Coastal Mixing and Optics (CMO) experiment, carried out on the New England Shelf (NES) in 1996–1997, created an extensive data set to study the mixing processes in shelf seas. Analyses of this data set have

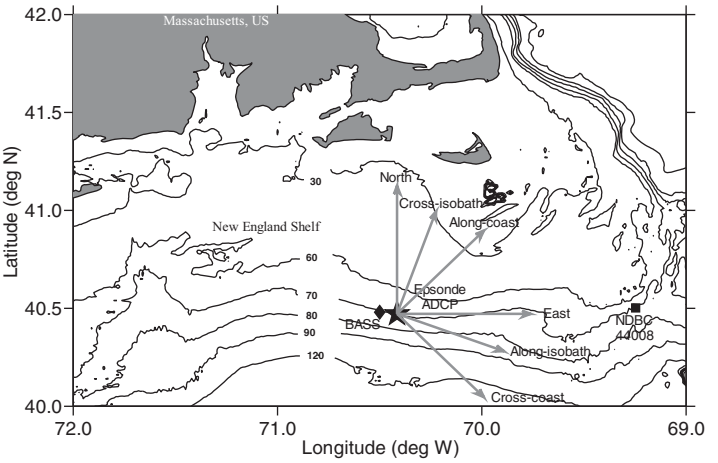

Figure 1. Map of study site with isobaths contoured in meters. Locations of EPSONDE and VM-ADCP are marked by a pentagram, BASS by a diamond, and NDBC 44008 by a square, respectively. Three sets of coordinates (north and east, along and cross-isobath, and along and cross-coast) are denoted by grey arrows.

already revealed the characteristics of mixing in the interior water column. *MacKinnon and Gregg* [2003a, 2003b, 2005a, 2005b] studied internal waves and related dissipation based on observations made in the late summer of 1996. They also showed the evolution of internal waves in response to local forcing, and the impact of mixing on water mass properties in the spring of 1997. Low levels of turbulent dissipation and diffusivity in the interior water column have been derived from microstructure [*Oakey and Greenan*, 2004] and dye releases [*Ledwell et al.*, 2004].

The present study builds on the understanding of dynamics and mixing characteristics of the NES from previous analyses of the CMO data set. We further analyze the data set with an objective to reveal a comprehensive view of layered mixing, from the interior water column to the BBL. The time variation of layered mixing will be illustrated and the linkage to flow and stratification conditions will be discussed. Novel aspects of the present study are (1) to distinguish and discuss the different characteristics of turbulence in the interior under stably stratified conditions and in the BBL under shear instability; (2) to evaluate the parameterization of internal wave mixing with the CMO data; and (3) to focus on understanding the variation of BBL mixing associated with shelf slope, stratification, tidal and subtidal flows.

The remainder of this paper is organized as follows: field observations and the associated data processing are described in Section 2; Section 3 and Section 4 present analysis of observational data to examine the layered thermohaline structures and mixing dynamics, respectively; the conclusions from this study are summarized in Section 5.

2. Field Observation and Data Processing

During 8–11 August 1997, measurements were made on the NES onboard R/V Oceanus near the 70 m isobath south of Nantucket, Massachusetts (Figure 1). Our date convention is that local noon 1 January is yearday 0.5.

2.1. Microstructure and CTD

Microstructure data were obtained from the EPSONDE profiler [*Oakey*, 1988], a 2.4 m tethered instrument ballasted to free-fall typically at 0.8 m s^{-1}. The microstructure sensor suite included a cold-film platinum thermometer (response time of 2 ms), a fast-tip thermistor (response time of 12 ms) and two custom-built airfoil shear probes to measure the velocity gradient profile. The thermistor was sampled at 128 Hz and the other three microstructure sensors were sampled at 256 Hz. EPSONDE was also equipped with a conventional Conductivity-Temperature-Depth (CTD) sensor.

EPSONDE casts used for this analysis were obtained along two 4 km lines in the east-west (approximately along-isobath) direction, and included up to twelve casts per occupation of the line over a period of about 2 h [see *Oakey and Greenan*, 2004, Figure 6]. The microstructure profiles collected during one line occupation were averaged to provide a single estimate for that time period. Measurements were conducted from yeardays 219.46 to 220.43 (1102 on 8 August to 1019 on 9 August 1997) along the first line and from yeardays 221.72 to 222.63 (1716 on 10 August to 1507 on 11 August 1997) along the second line. For convenience, the two periods are referred to as day 1 and day 2, respectively. EPSONDE profiles either finished on

the seabed or close to the bottom, in order to resolve mixing in the BBL. A guard ring at the leading end of the instrument protected the microstructure probes. The processing methodology for EPSONDE data was detailed by *Oakey and Greenan* [2004].

2.2. VM-ADCP

The R/V Oceanus was equipped with a 300 kHz broad band vessel mounted-acoustic Doppler current profiler (VM-ADCP), which measured the velocity over the depths of 11–57 m above the bottom (mab) with a vertical bin size of 2 m. Each VM-ADCP velocity profile was derived by averaging pings over a 10 min period. Velocity vectors are rotated to along and cross-isobath directions with positive x toward 110°T (clockwise from north orientation, the same hereinafter) and positive y toward 20°T (Figure 1). The VM-ADCP velocity is also used to estimate vertical shear variance ($S^2 = S_u^2 + S_v^2 = (\partial u/\partial z)^2 + (\partial v/\partial z)^2$, where u and v are along and cross-isobath velocity, respectively; z is the vertical coordinate). The triangular weighting function used by the RDI ADCP instruments results in adjacent depth bins not being independent because of overlapping measurements; therefore, vertical shear has been calculated by first differencing over 4 m intervals. The gradient Richardson number (Ri) at 11–57 mab is calculated according to $Ri = N^2/S^2$, where N^2 is buoyancy frequency squared from the EPSONDE CTD and S^2 is shear variance from the VM-ADCP.

2.3. BASS

The Benthic Acoustic Stress Sensor (BASS) tripod was located about 7 km west of the EPSONDE survey site. The tripod consisted of a vertical array of six BASS sensors at 0.74, 1.1, 2.2, 3.3, 5.4, and 7.0 mab which were sampled at 1.2 Hz in bursts. Each sensor enables the computation of a three-dimensional velocity vector by measuring the differential travel time of acoustic pulses traveling in opposite directions along four 15 cm acoustic axes. In each 2 h cycle, measurements were made during three bursts, each burst lasting half an hour, followed by half an hour during which the instruments were idle [*Shaw et al*., 2001]. Vertical profiles of velocity are obtained by fitting second-order polynomial functions to the nonevenly distributed velocities obtained from the six sensors. Shear is calculated from the derivatives of the fitted polynomials (to be presented in section 4.1). Ri is calculated by combining N^2 from EPSONDE and S^2 from BASS. Estimates of Reynolds stress ($<u'w'>$ and $<v'w'>$) are obtained by computing eddy correlation from velocity of each burst. A linear filter and differencing technique are used to remove contamination on the estimation of Reynolds stress by surface waves [*Shaw and Trowbridge*, 2001]. Estimates of ε are obtained from BASS by fitting theoretical models of inertial subrange turbulence to measured spectra. ε estimated from BASS is discussed in section 4.3 and its variation broadly follows that from EPSONDE. Detailed data processing procedures for estimating Reynolds stress and ε from BASS were described by *Shaw and Trowbridge* [2001] and *Shaw et al*. [2001].

2.4. Wind Forcing

Wind data are obtained from measurements on buoy 44008 from the National Data Buoy Center (NDBC), which was located 85 km to the east of the EPSONDE site. Previous studies demonstrated that the subtidal along-isobath flow has the highest correlation with the component of wind stress parallel to the southern New England coastline [*Beardsley et al*., 1985; *Shearman and Lentz*, 2003], according to the conceptual model of *Boicourt and Hacker* [1976]. Following these studies, the along-coast wind is defined positive toward 45°T (Figure 1). Wind stress is averaged over 1 h intervals.

3. Layered Stratification

3.1. Overview

Following *Wright* [1976] and *Lentz et al*. [2003], water with salinity less than 32.50 is defined as "shelf water" and that with salinity greater than 33.50 is referred to as "shelf-slope front water." This also maintains consistency with the observed characteristics of temperature (T) and salinity (S) shown in Figure 2a. The relative contribution of temperature and salinity to the growing vertical density gradient over the measurement period is quantified by the spice gradient, defined as:

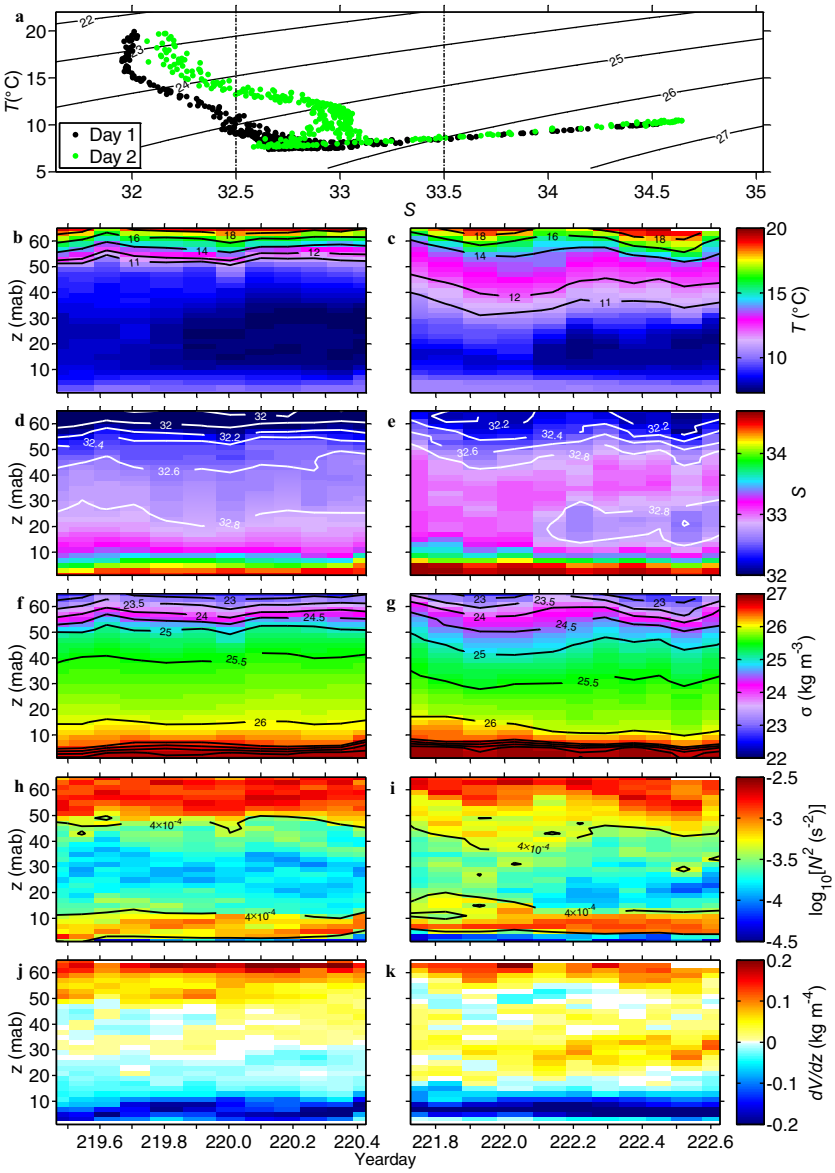

Figure 2. (a) Temperature-salinity diagram with contours of potential density, day 1 in black and day 2 in green. Time-depth variations of (b, c) temperature (T); (d, e) salinity (S); (f, g) potential density (σ); (h, i) squared buoyancy frequency (N^2); and (j, k) spice gradient (dV/dz) on day 1(Figures 2b, 2d, 2f, 2h and 2j) and day 2 (Figures 2c, 2e, 2g, 2i, and 2k). Units of depth are meters above the bottom (mab).

$$\frac{dV}{dz} = \alpha\rho\frac{\partial T}{\partial z} + \beta\rho\frac{\partial S}{\partial z}, \tag{1}$$

where ρ is density, α is the thermal expansion coefficient and β is the saline contraction coefficient. The values (mean $\pm$ standard deviation) of α and β are $\alpha = 1.67\times10^{-4} \pm 3.11\times10^{-6}\ ^{\circ}C^{-1}$, $\beta = 7.60\times10^{-4} \pm 5.75\times10^{-7}$ based on T, S and pressure [*McDougall*, 1987].

The time-depth variations of T, S, potential density (σ), N^2 and spice gradient on day 1 and day 2 are shown in Figures 2b–2k. The ensemble averages of T, S, σ and N^2 are shown in Figure 3. The vertical distributions of the above variables reveal a four-layer structure. Taking $N^2 = 4\times10^{-4}\ s^{-2}$ as a critical value, the four layers are defined as: the subsurface stratification layer with $N^2 > 4\times10^{-4}\ s^{-2}$; the middepth weak stratification layer with $N^2 < 4\times10^{-4}\ s^{-2}$; the lower stratification layer with $N^2 > 4\times10^{-4}\ s^{-2}$ and the well-mixed BBL with $N^2 < 4\times10^{-4}\ s^{-2}$. A possible well-mixed surface layer was not observed because EPSONDE did not provide data in the upper 5 m of the water column. The observed upper three layers are hereafter referred to as midcolumn layers, for convenience.

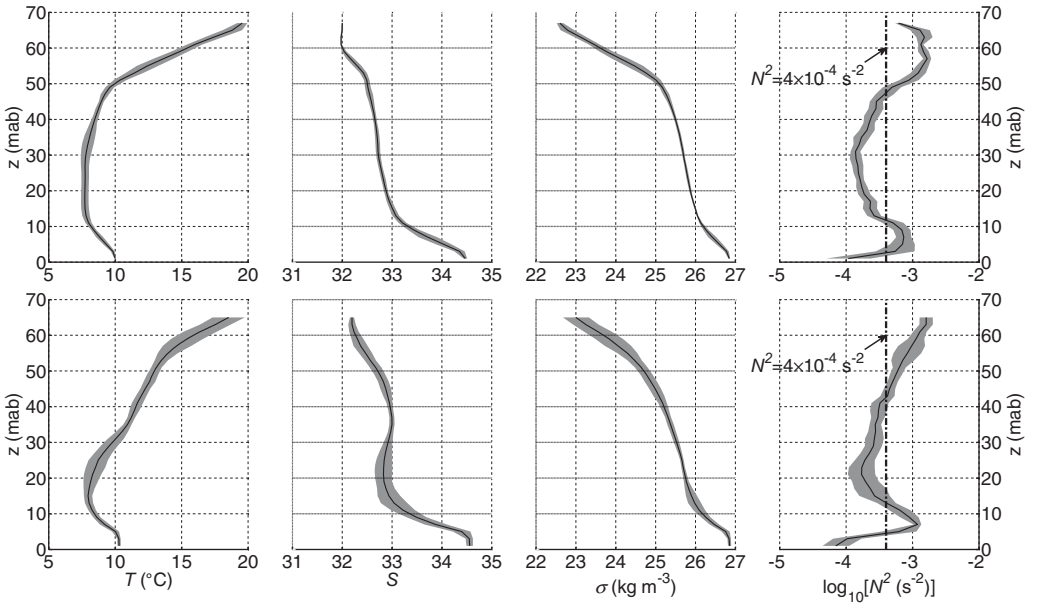

Figure 3. (left to right) Vertical profiles of temperature (T); salinity (S); potential density (σ) and squared buoyancy frequency (N^2) on (top) day 1 and (bottom) day 2. The dash-dotted lines denote $N^2=4\times10^{-4}$ s^{-2}. The solid curves are the ensemble averages and the shaded areas show the ranges of standard deviations.

3.2. Subsurface Stratification and Middepth Stratification

The subsurface stratification layer and middepth weak stratification layer covered the water column above 12 mab. The interface of the two layers was located at about 48 mab on day 1 and descended to about 40 mab on day 2. With increasing depth, temperature in the upper 10 m of the water column decreased from about 20°C to 15°C; salinity was nearly uniform with a value of 32.00 on day 1 and with at value of 32.20 on day 2. Hence, the density gradient in the upper 10 m was mainly driven by temperature (yellow and red patches in Figures 2j–2k).

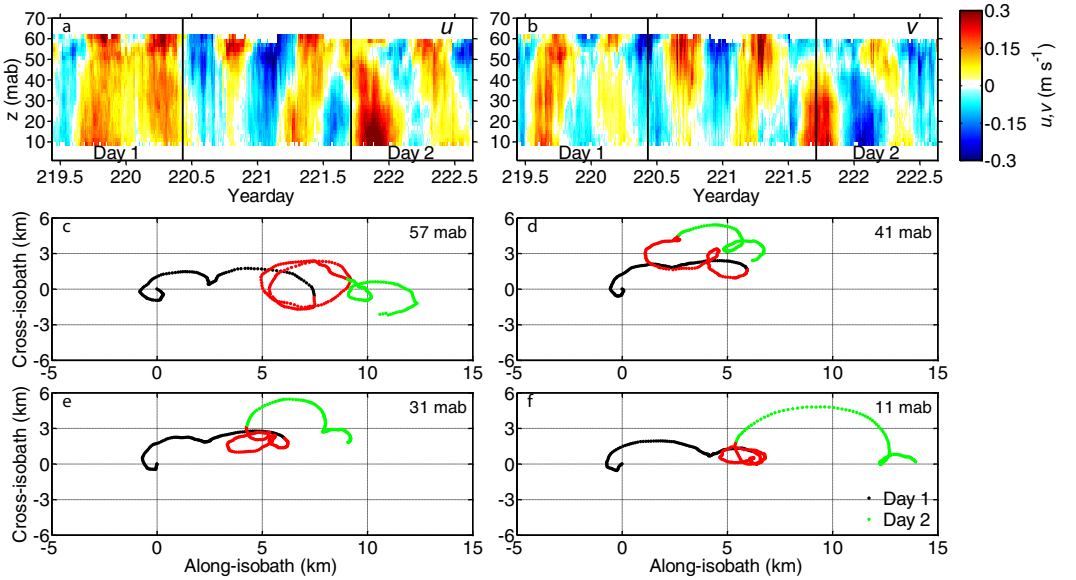

Figure 4. Time-depth variations of (a) along (u) and (b) cross-isobath (v) velocities. (c–f) The progressive current vectors (time-integrated displacements) at 57, 41, 31, and 11 mab during yeardays 219.44–222.63. Displacements on day 1, day 2 and the 1 day gap between them are denoted in black, green and red, respectively.

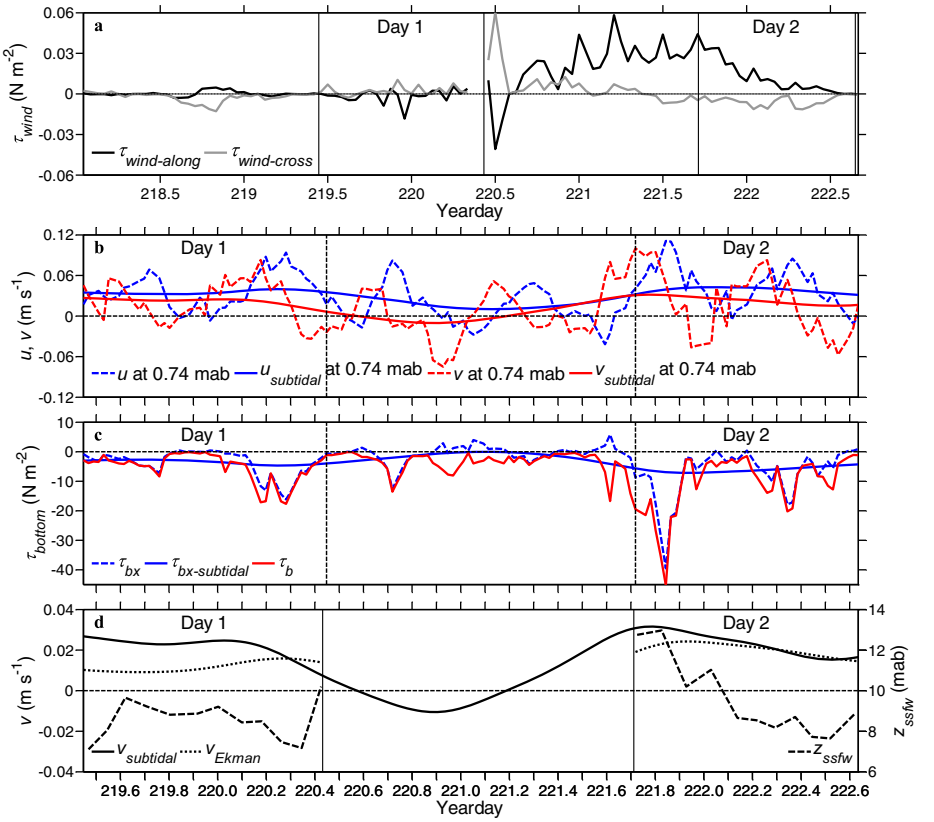

Figure 5. Time series of (a) the along (τ_{along}) and cross-coast (τ_{cross}) wind stress at sea surface; (b) along (u) and cross-isobath (v) velocities at 0.74 mab and their subtidal component ($u_{subtidal}$, $v_{subtidal}$); (c) total bottom stress (τ_b), along-isobath bottom stress (τ_{bx}) and its subtidal component ($\tau_{bx\text{-}subtidal}$); (d) $v_{subtidal}$, Ekman component of cross-isobath velocity (v_{Ekman}) and the height of shelf-slope front water (z_{ssfw}).

In the depth range of 12–60 mab, the temperature ranged from 8 to 15°C with a notable increase of 1–4°C from day 1 to day 2. Salinity ranged 32.00–33.00 with an increase of 0.50 from day 1 to day 2. The density gradient was mainly influenced by temperature, but occasionally was controlled by salinity (blue patches in Figures 2j–2k). Near the site of the EPSONDE measurements, temperature and salinity gradients in the cross-isobath direction have been well documented [*Lentz et al*., 2003]. *Lentz* [2010] also showed that there existed a temperature gradient in the along-isobath direction, increasing from southeast to northwest. Figure 4 shows the time-depth variations of velocities and progressive vector diagrams at four selected heights above the seabed. Besides the periodic tidal component, the along and cross-isobath velocities both revealed subtidal motions. The maximum displacements were less than 3 km in the cross-isobath direction and 7–13 km eastward in the along-isobath direction.

Time series of the height of density isopycnals (e.g., 25.0 kg m^{-3}) show fluctuations with approximately semidiurnal periods (Figures 2f–2g). Their amplitudes from crest to trough are about 3 m on day 1 and 10 m on day 2, corresponding to small and large variability of the ensemble averages of temperature, salinity and density on day 1 and day 2, respectively (Figure 3).

3.3. Lower-Layer Stratification and Well-Mixed BBL

The lower stratification layer and the well-mixed BBL were confined below 11 mab on day 1 and 14 mab on day 2. The interface of the two layers was located at 3 mab on day 1 and 5 mab on day 2. With increasing depth, stable density profiles in these two layers were related to salinity increasing from 33.00 to 34.50, while temperature increased from 8 to 10°C. The density gradient in the stratification layer was controlled primarily by salinity (Figures 2j–2k).

High salinity water with $S>33.50$ in these two layers originated from the shelf-slope front water. Previous studies on the NES [*Boicourt and Hacker*, 1976; *Houghton et al*., 1988] suggested that onshore movement of the shelf-slope front water was related to the eastward along-coast wind stress. *Lentz et al*. [2003] quantified

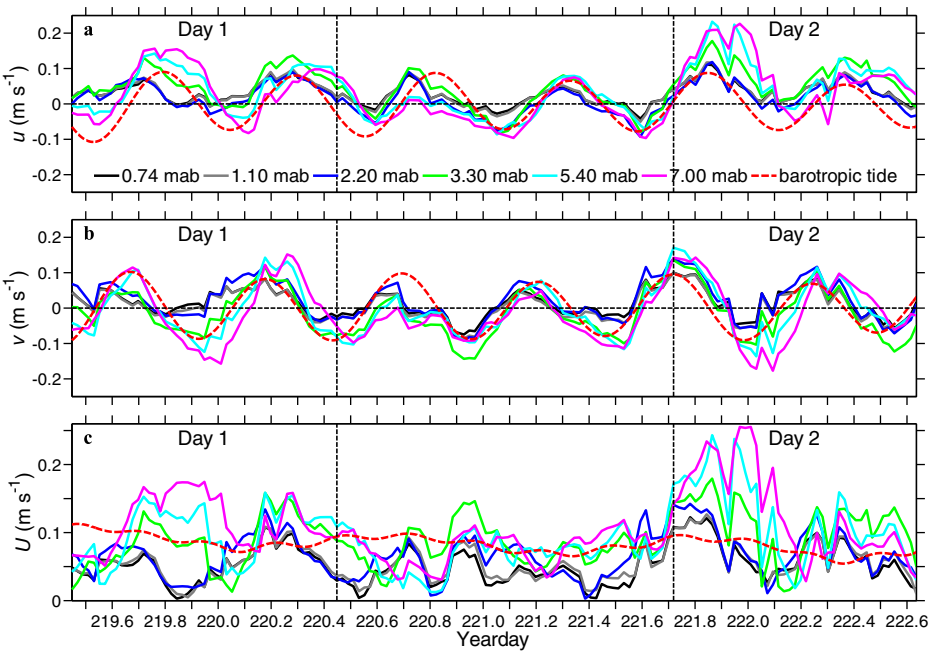

Figure 6. Time series of (a) along (*u*) and (b) cross-isobath (*v*) velocities; and c) flow speed (*U*) obtained from BASS at 0.74, 1.10, 2.20, 3.30, 5.40, and 7.00 mab, as well as barotropic tidal velocities (red dashed lines) calculated with OTIS.

this relationship based on CMO measurements from August 1996 to June 1997. They found that an eastward along-coast wind stress greater than 0.2 N m^{-2} drives an eastward along-isobath current throughout the water column, resulting in a westward bottom stress that forces a northward cross-isobath Ekman transport and, hence, onshore displacement of shelf-slope front water at the foot of shelf-slope.

Figures 5a–5c shows the time series of observed along and cross-coast wind stresses (τ_{along} and τ_{cross}), along and cross-isobath velocities (*u* and *v*) and their subtidal component ($u_{subtidal}$ and $v_{subtidal}$) at 0.74 mab, along-isobath bottom stress (τ_{bx}) and its subtidal component ($\tau_{bx\text{-}subtidal}$). The subtidal values of *u*, *v* and τ_{bx} are obtained by applying low-pass filter with a cutoff of 33 h. $v_{subtidal}$ was in the northward direction on day 1 and day 2, which displaced the shelf-slope front water onshore and resulted in the lower-layer stratification. Near bottom $v_{subtidal}$ was linked to $\tau_{bx\text{-}subtidal}$ through the bottom Ekman dynamics:

$$v_{Ekman} = \frac{\tau_{bx-subtidal}}{\rho f \delta_b}, \tag{2}$$

where v_{Ekman} is the Ekman component of *v*; *f* is the Coriolis parameter and δ_b is the height of Ekman layer, taken as the average BBL height (~3 m). Figure 5d shows that the time series of $v_{subtidal}$, v_{Ekman} and the height of shelf-slope front water (z_{ssfw}, with $S>33.50$). On day 1 v_{Ekman} and $v_{subtidal}$ varied slightly and z_{ssfw} was at about 7–10 mab; on day 2 v_{Ekman} and $v_{subtidal}$ decreased from 0.03 to about 0.015 m s^{-1} and z_{ssfw} decreased from 13 to about 8 mab. During our measurements and one day preceding the measurements, τ_{along} was primarily in the eastward direction with a mean magnitude of 0.02 N m^{-2} and τ_{cross} was generally weak. According to *Lentz et al*. [2003], this wind stress is not strong enough to produce eastward $u_{subtidal}$ and resultant $\tau_{bx\text{-}subtidal}$. Therefore, $u_{subtidal}$ must be related to cross-shore pressure gradient.

The time series of *u*, *v* and flow speed (*U*) obtained from the BASS at 6 levels, along with the corresponding barotropic tidal velocities, are shown in Figure 6. The barotropic tidal velocities are calculated using the Oregon State University Tidal Inversion Software (OTIS) [*Egbert and Erofeeva*, 2002]. In comparison with the barotropic tidal flow, the observed along-isobath velocity at each of the six levels of the BASS contains an eastward subtidal component, similar to the flow observed by the VM-ADCP (Figure 4). The signs of *v* oscillate; but for the lower three levels the magnitudes of onshore flow are larger than that of the offshore flow. This suggests a subtidal onshore flow that can be related to the bottom Ekman transport induced by the subtidal eastward current.

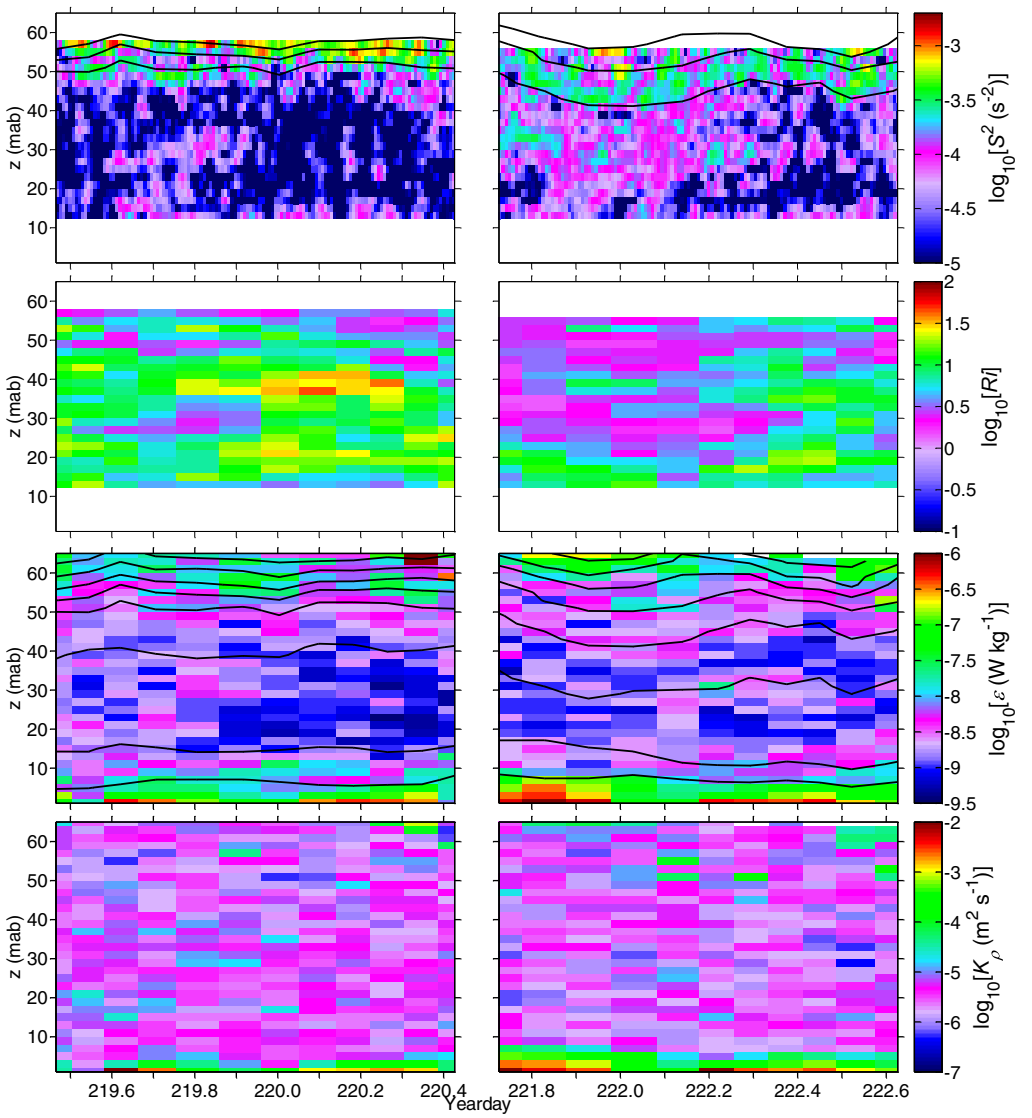

Figure 7. (top to bottom) Time-depth variations of shear variance (S^2) overlaid with isopycnals of 24.0–25.0 kg m^{-3} with an interval of 0.5 kg m^{-3}; gradient Richardson number (Ri); TKE dissipation (ε) overlaid with isopycnals of 22.0–26.5 kg m^{-3} with an interval of 0.5 kg m^{-3} and eddy diffusivity (K_ρ), on (left) day 1 and (right) day 2.

4. Layered Turbulent Mixing

4.1. Overview

Figure 7 shows the time-depth variations of S^2, Ri, ε, and eddy diffusivity ($K_\rho = 0.2\varepsilon/N^2$) based on VM-ADCP and EPSONDE measurements. Figure 8 shows the supplement of S^2, N^2, Ri, ε and the TKE production rate (P) in the BBL and the adjacent part of the lower stratification layer, based on BASS and EPSONDE measurements. Vertical distributions of the ensemble averages and standard deviations of S^2, Ri, ε and K_ρ throughout the water column are displayed in Figure 9. For the upper two layers, strong shear variance with $S^2 > 10^{-4}$ s^{-2} occurred above 50 mab on day 1, and split into two regions on day 2: a layer above 40 mab and a patch between 20 and 40 mab during first half of day 2. However, in the range of 11–57 mab resolved by the VM-ADCP, the presence of stratification led to $Ri > 1$, suggesting that strong turbulence was generally damped by stratification, consistent with observed weak ε of 10^{-9}–10^{-8} W kg^{-1} and weak K_ρ of 10^{-6}–10^{-5} m^2 s^{-1} in this layer. There are some scattered areas with enhanced ε above 10^{-8} W kg^{-1} in the upper 10 m; however, an estimate of Ri is not available because of the lack of VM-ADCP data.

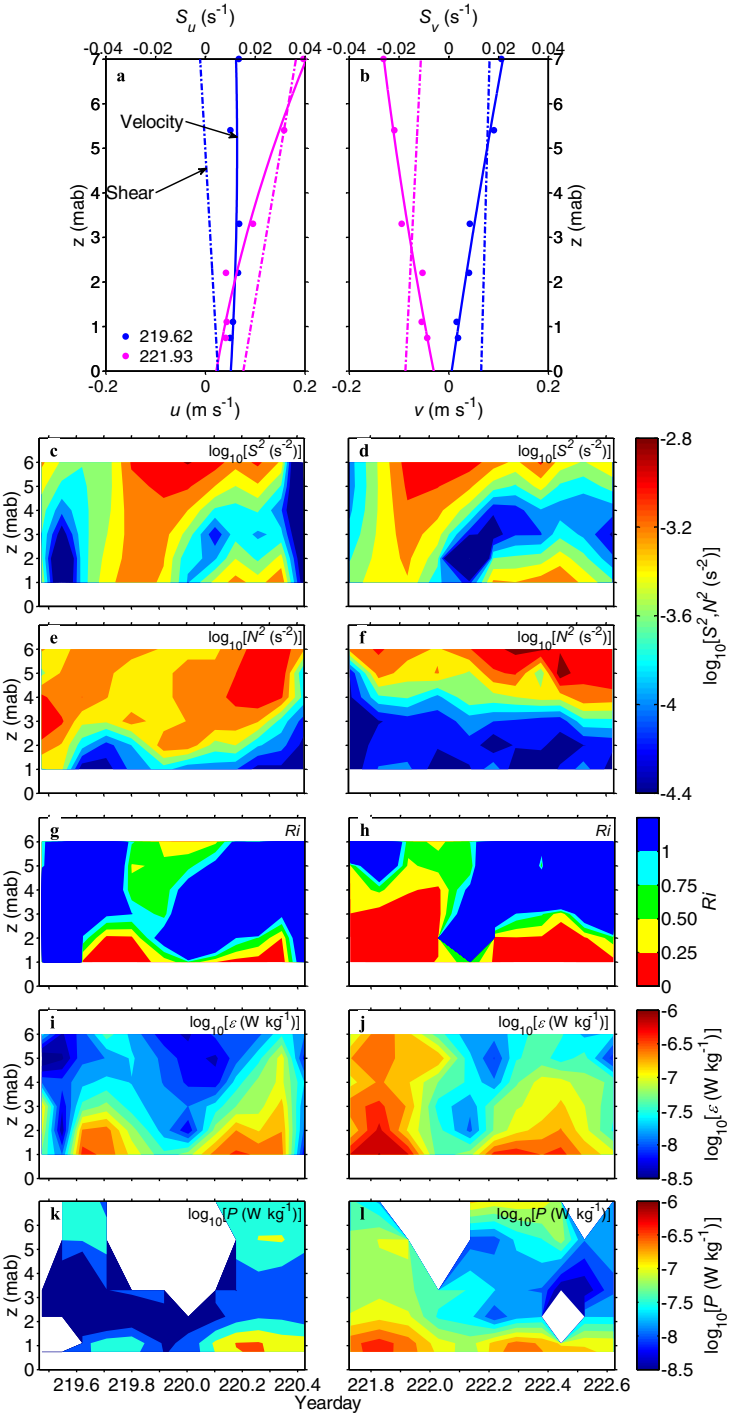

Figure 8. (a, b) Two samples of observed velocity profiles (solid circles), their second-order polynomial fits (solid lines) and the inferred shear (dash-dotted lines). Time-depth variations of (c, d) shear variance (S^2), (e, f) squared buoyancy frequency (N^2); (g, h) gradient Richardson number (Ri); (i, j) TKE dissipation rate (ε); and (k, l) TKE production rate (P) in the lower part of the lower stratification layer and the BBL. (left) Figures 8c, 8e, 8g, 8i and 8k and (right) Figures 8d, 8f, 8h, 8j and 8l for day 1 and day 2, respectively.

For the lower two layers, shear is calculated by velocities measured by BASS. Figures 8a–8b shows two sample velocity profiles, their second-order polynomial fits and the inferred shear. The fits are quite accurate, as suggested by the small normalized root-mean-square error ($NRMSE = \frac{\sqrt{\frac{1}{n}\sum_1^n (Vel_{obs} - Vel_{fit})^2}}{max(Vel_{obs}) - min(Vel_{obs})}$, where Vel is velocity, n is the number of data values, $max(Vel_{obs})$ and $min(Vel_{obs})$ are the maximum and minimum of observed velocities, respectively.) between the observed and fitted velocities, 4.3% for u and 3.5% for v. High values of ε up to 10^{-6} W kg^{-1} and K_ρ up to 10^{-3} m^2 s^{-1} were observed in the BBL, corresponding well with $Ri<0.25$. The occurrence of $Ri<0.25$ in the BBL was always observed to be associated with strong shear. On the other hand, while large shear was also measured outside the BBL, strong stratification in that region inhibited the occurrence of shear instability, leading to low values of $\varepsilon<10^{-7}$ W kg^{-1} and $K_\rho<10^{-5}$ m^2 s^{-1}.

Figure 9 clearly shows that variability in Ri corresponds well with strong and weak ε in the BBL and midcolumn layers. This is consistent with the classical understanding of weak velocity fluctuations under stable condition of $Ri>0.25$ and instabilities leading to active turbulence for $Ri<0.25$ [*Miles*, 1961; *Howard*, 1961; *Rohr et al.*, 1988]. Hence, the mixing characteristics showed mainly a two-layered structure: the midcolumn layer with stably stratified conditions and the BBL under shear instability. The distinction of the two layers can be further revealed by the scatter diagrams of Ri versus ε, N^2 versus ε, S^2 versus ε and N^2 versus S^2 (Figure 10). The number of data samples corresponding to $Ri<0.25$ is small. Besides $Ri<0.25$, Ri values in the range of 0.25–0.5 are

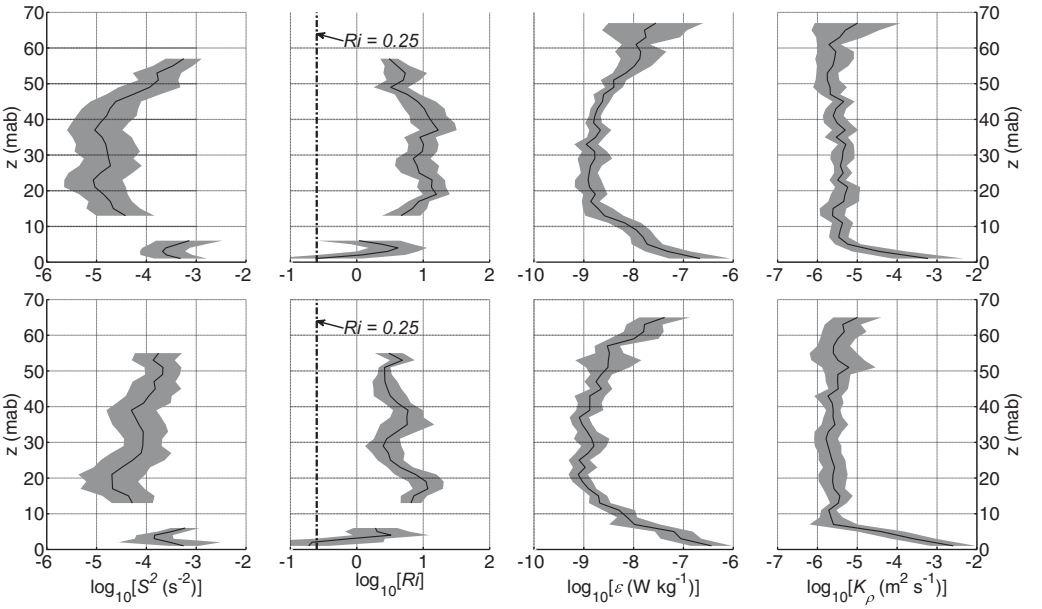

Figure 9. Same as Figure 3 but for (left to right) shear variance (S^2); gradient Richardson number (Ri); TKE dissipation rate (ε) and eddy diffusivity (K_ρ). The ensemble averages are based on median. The dash-dotted lines denote $Ri=0.25$.

mostly distributed in the BBL (yellow patches in Figures 8g–8h, with the exception of one value outside the BBL around yearday 220.0). We thus select N^2, S^2 and ε values corresponding to $Ri<0.5$ to represent the bottom-affected water. Ri values in the range of 0.5–1 are also only located at heights of 1–6 mab (green and cyan patches in Figures 8g–8h), with some distributed in the BBL and others in the lower stratification layer. We thus select N^2, S^2 and ε values corresponding to $Ri>1$ to represent the midcolumn water. By separating data values in such a way, in midcolumn water ($Ri>1$) and the bottom-affected water ($Ri<0.5$), ε has a poor ($r=-0.38$) and moderate ($r=-0.53$) correlation with Ri, respectively (Figure 10a). Correlations between N^2 and ε in the midcolumn and bottom-affected waters have opposite signs: stratification provides positive

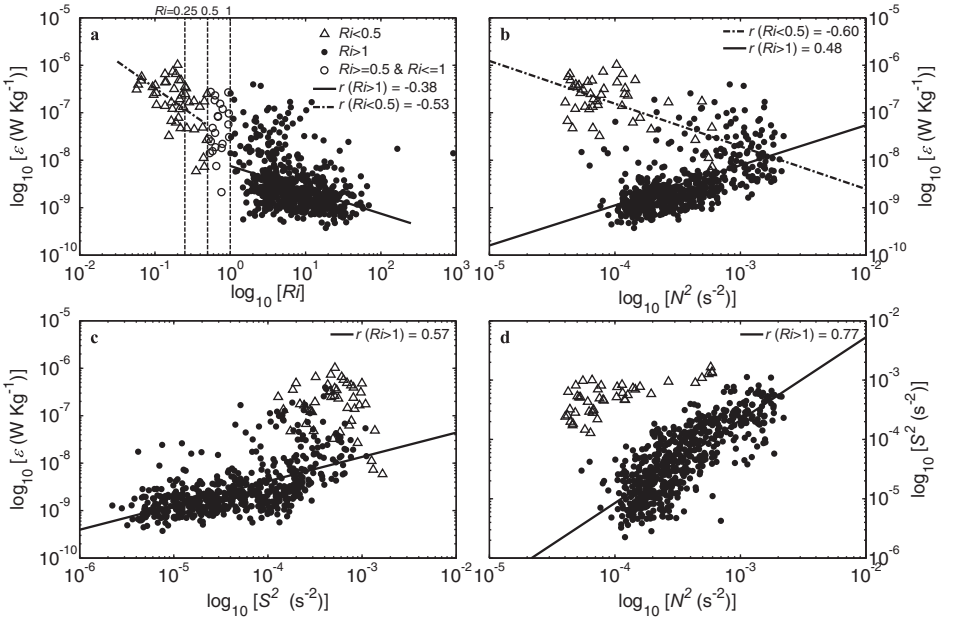

Figure 10. Scatter diagrams of observed TKE dissipation versus (a) gradient Richardson number (Ri), (b) squared buoyancy frequency (N^2), and (c) shear variance (S^2). d) Scatter diagrams of N^2 versus S^2. Values corresponding to $Ri>1$ and $Ri<0.5$ are denoted by solid circles and hollow triangles, respectively. Solid and dashed lines represent the best linear fits of the data.

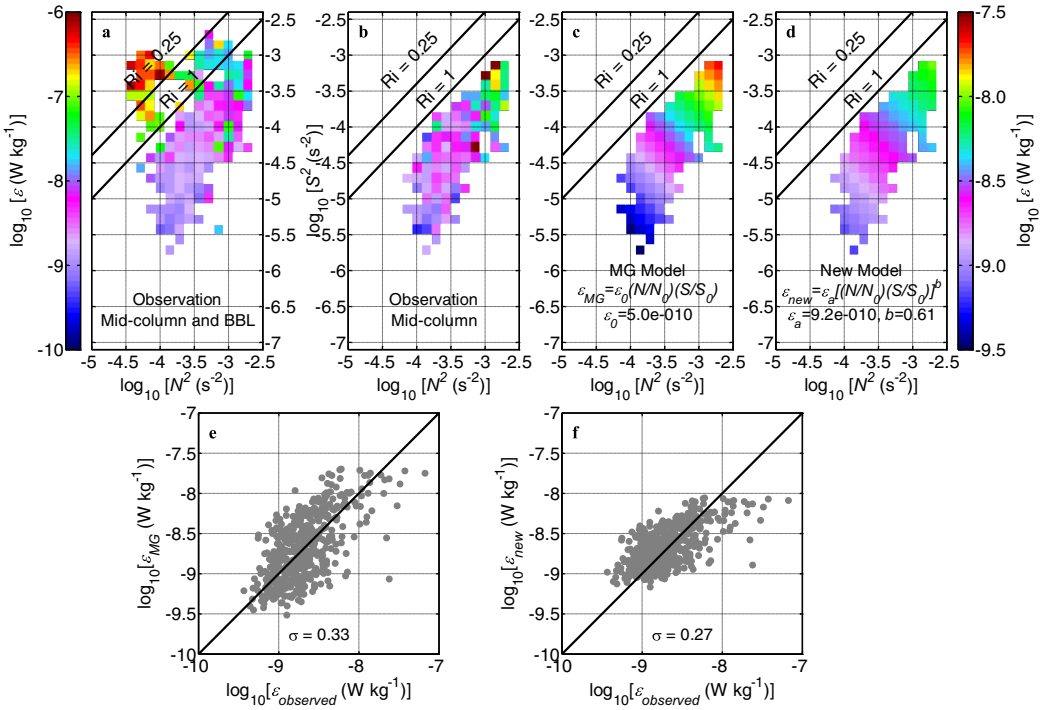

Figure 11. (a–d) The distribution of TKE dissipation rates (ε, color coded) as functions of stratification (N, x axis) and shear (S, y axis). (a) The observed values in the midcolumn and BBL with the color axis of ε denoted on its left. (b) The observed values in the midcolumn. (c, d) The fits of the observed ε in midcolumn to the original and a slightly modified MG model, respectively. The color axis on the right applies to Figures 11b–11d. (e, f) Scatterplots of observed TKE dissipation rates ($\varepsilon_{observed}$) versus modeled TKE dissipation rates according to equation (3) (ε_{MG}) and equation (5) (ε_{new}) with the straight lines depicting the 1:1 ratio.

contribution to ε in the midcolumn layers (r=0.48) and negative contribution to ε in the bottom-affected layers (r=−0.60; Figure 10b). The contributions of S^2 to ε differ in the midcolumn and the boundary. With S^2 increasing from 10^{-6} to 10^{-3} s^{-2}, ε in the midcolumn water increases simultaneously; S^2 and ε have a correlation of r=0.57. The bottom-affected ε exhibits little dependence on S^2 (Figure 10c). S^2 and N^2 are correlated (r=0.77) in the midcolumn water but not in the bottom-affected water (Figure 10d).

4.2. Midcolumn Turbulence

Following *MacKinnon and Gregg* [2003b], the observed values of ε are grouped according to bins of S^2 and N^2, which are spaced evenly on logarithmic axes. The average value of ε for each bin is calculated only if at least five values are contained in that bin. To reduce the bias introduced by the different vertical resolutions, N^2 and ε were vertically averaged over the 2 m VM-ADCP bins. Since large scale shear comes from low frequency motions [*MacKinnon and Gregg*, 2003b], VM-ADCP data were low-pass filtered with cutoff frequency 0.17 cph before computing the shear. Figure 11a displays the distributions of all of the observed ε values, including the midcolumn and the bottom-affected layers. The general tendency is that ε increases with diminishing stability (Ri). This can be regarded as the first-order process for shelf mixing. Figure 11b displays the distribution of observed ε values only in the midcolumn. It shows the tendency of ε increasing with increasing S^2 and increasing N^2, which can be regarded as the second-order process for shelf mixing.

The relatively weak ε in the midcolumn is important for fluxes across the pycnocline. Classical turbulent closure models, e.g., second-order turbulent closure models of *Mellor and Yamada* [1974, 1982] and *Canuto et al*. [2001], predict the dependence of ε on stability functions, which rely on shear and buoyancy-related nondimensional parameters and can be often described as functions of Ri when a local equilibrium is assumed [*Burchard et al*., 2008]. Variation of ε obtained by such models may be consistent with observations under condition of shear instability but not under stable conditions according to the fine-scale Ri [*Simpson et al*., 1996; *Burchard et al*., 2008; *Palmer et al*., 2013]. The observed data fit a parameterized model for shelf

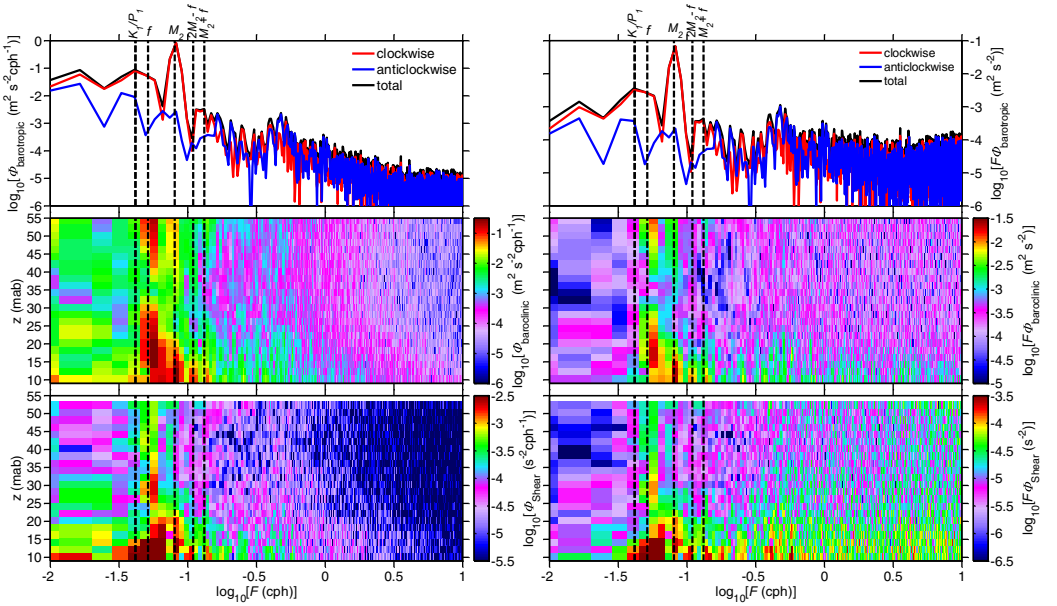

Figure 12. (top) Rotary energy spectra of barotropic velocity showing clockwise (red), anticlockwise (blue) components and the total (black). Vertical distributions of rotary total energy spectra (clockwise plus anticlockwise) of (middle) baroclinic velocity and (bottom) shear. (left) Spectral density and (right) the energy-preserving spectra, respectively. Vertical lines mark the frequencies of diurnal solar tide (K_1/P_1), local inertial (f), semidiurnal lunar tide (M_2), and oscillations resulted from nonlinear interactions (M_2+f and $2M_2-f$).

internal wave turbulence better, proposed by *MacKinnon and Gregg* [2003b, hereafter referred as MG model), that takes the form of

$$\varepsilon_{MG}=\varepsilon_0\left(\frac{N}{N_0}\right)\left(\frac{S}{S_0}\right). \tag{3}$$

The MG model contains three tuning parameters N_0, S_0 and ε_0. By setting $N_0=S_0=3$ cph, the fitting of the MG model to the observed ε in the midcolumn yields $\varepsilon_0=5.0\times10^{-10}$ W kg^{-1}. Figure 11c shows the MG model fitted distribution of ε. The similarity between Figure 11b and Figure 11c suggests that the MG model describes the distribution of observed ε in midcolumn reasonably well.

The nature of internal waves can be explored by examining the rotary energy spectra of barotropic velocity (depth mean velocity), baroclinic velocity (total minus depth mean velocity) and shear (Figure 12), and time series of baroclinic velocity and kinetic energy (Figure 13). The barotropic energy is dominated by the clockwise rotating component with peaks primarily at the semidiurnal lunar tidal frequency (M_2) and secondarily at the diurnal solar tidal frequency (K_1/P_1). This maintains consistency with the results of *Shearman and Lentz* [2004] from analyses of velocity measured from moorings from August 1996 through June 1997 on the NES. The energy spectra of baroclinic velocity and shear vary with depth. Above 15 mab, the spectra of baroclinic velocity show a primary peak at the near-inertial frequency (f) and a secondary peak at the M_2 frequency. Below 15 mab, the primary peak shifts to M_2 frequency. The shear spectra have a peak at the near-inertial frequency and the contribution from M_2 frequency is only evident below 20 mab. Below 15 mab, the baroclinic velocity and shear spectra also show peaks at frequencies of M_2+f and $2M_2-f$, suggesting the contribution from nonlinear interaction between the near-inertial and M_2 internal waves here. Overall, the above analyses suggest that the midcolumn mixing can be related to near-inertial and semidiurnal internal waves. The near-inertial waves are usually setup by abrupt changes in wind direction [*van Haren et al*., 1999] or wind magnitude [*Rippeth et al*., 2002]. Figure 5 shows that the along and cross-coast winds were generally weak on day 1, and increased to 0.06 N m^{-2} during the 1 day gap between days 1 and 2, and then gradually dropped to nearly zero at the end of day 2. From day 1 to day 2, the intensity of internal waves was enhanced, as is evident both in baroclinc velocity (Figures 13a and 13b) and depth-averaged baroclinic energy ($E_{baroclinic}=\frac{1}{n}\sum_1^n\frac{u_{bc}^2+v_{bc}^2}{2}$, where u_{bc} and v_{bc} are observed along and cross-isobath baroclinic (total

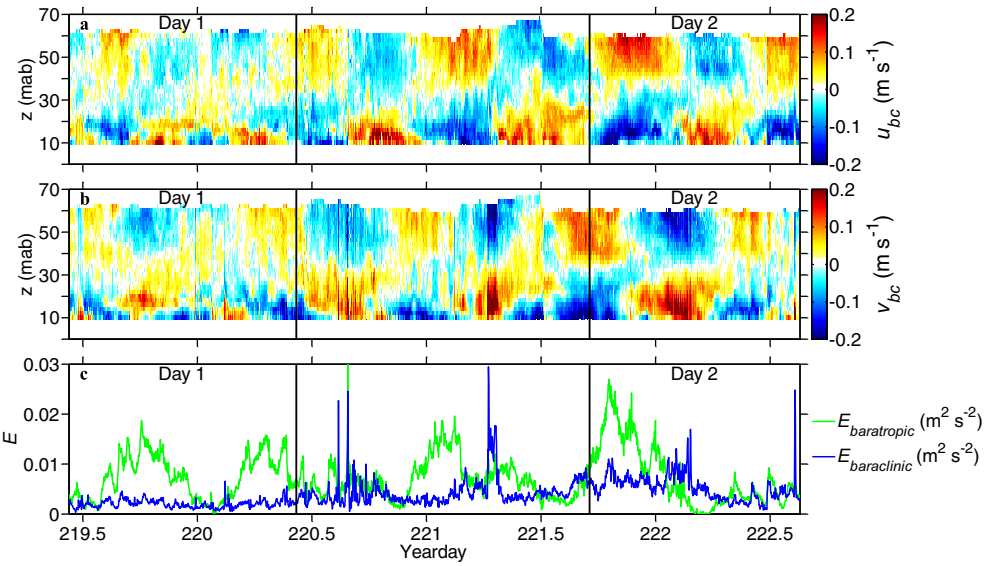

Figure 13. Time-depth variations of (a) along (u_{bc}) and (b) cross-isobath (v_{bc}) baroclinic velocities. (c) Time series of depth-averaged barotropic ($E_{barotropic}$, green) and baroclinic ($E_{baroclinic}$, blue) kinetic energy.

minus depth-mean) velocities, respectively; n is the number of VM-ADCP layers., Figure 13c). On the other hand the averaged barotropic energy in the 2 days was almost the same ($E_{barotropic}=\frac{u_{bt}^2+v_{bt}^2}{2}$, where u_{bt} and v_{bt} are observed along and cross-isobath barotropic (depth mean) velocities, respectively, 0.0074 and 0.0075 m^2 s^{-2} in day 1 and day 2, respectively). Thus, the variation of internal wave energy was likely related to wind.

Van der Lee and Umlauf [2011] summarized eight previous studies that applied MG model for observed ε in interior water on continental shelves. They found that the fitted parameter ε_0 for different sites ranges over two orders of magnitude. Such a degree of scatter indicates that the MG model may not be suitable for all applications. In the following, we compare our data with two other data sets analyzed by *MacKinnon and Gregg* [2003b, hereafter referred to as MG03; 2005b, hereafter referred to as MG05]. The three data sets were all collected at nearby sites on the NES. The data set being presented in this paper and MG03's data were both collected in summer, but in different years. The two data sets show similar ranges of N^2, S^2 and ε, resulting in similar values of ε_0 ($\varepsilon_0=6.9\times10^{-10}$ W kg^{-1} for MG03 and $\varepsilon_0=5.0\times10^{-10}$ W kg^{-1} for our data). For MG05, measurements were made in spring during restratification; the range of ε is similar with MG03's and our data, but the magnitudes of N^2 and S^2 are 1–2 orders of magnitude smaller. This results in a two-fold decrease in ε_0 ($\varepsilon_0=1.1\times10^{-9}$ W kg^{-1} for MG05). According to these data sets from the same site on the NES, similar ranges of N^2 leads to similar ε_0 for MG model, and ε_0 decreases with increasing N^2. This is in agreement with the results of *van der Lee and Umlauf* [2011], who conducted measurements in 2008 (summer) and 2010 (winter) in Baltic Sea. Although the observations were made in different seasons and different years, N^2 of the two data sets have similar ranges, resulting in the similar values of ε_0 ($\varepsilon_0=1.5\times10^{-10}$ W kg^{-1} for summer of 2008; $\varepsilon_0=1.7\times10^{-10}$ W kg^{-1} for winter of 2010). It is conceivable that the relationship of ε_0 versus N^2 may be influenced by local bathymetric parameters (e.g., slope), since internal waves on continental shelves are strongly affected by local topography (e.g., internal wave propagation, scattering and reflection) [*Kunze and Smith*, 2004].

Another issue with the MG model is that the error of fitting it to observations can be significant. The range of ε estimated by the MG model may differ from the observed range [e.g., *van der Lee and Umlauf*, 2011; *Carter et al*., 2005]. For our data set, the range of ε_{MG} is larger than that of observed ε (Figure 11c). We define a measure of difference between the model estimated (ε_{model}) and observed ($\varepsilon_{observed}$) values according to

$$\sigma=\left[\frac{1}{n}\sum_{1}^{n}\left(\log_{10}\varepsilon_{model}-\log_{10}\varepsilon_{observed}\right)^2\right]^{1/2}, \quad (4)$$

where n is the number of data values. For our original observed data set (not averaged for combined bins of S^2 and N^2), by setting $\varepsilon_{model}=\varepsilon_{MG}$ (ε_{MG} is calculated according to equation (3) using original observed N

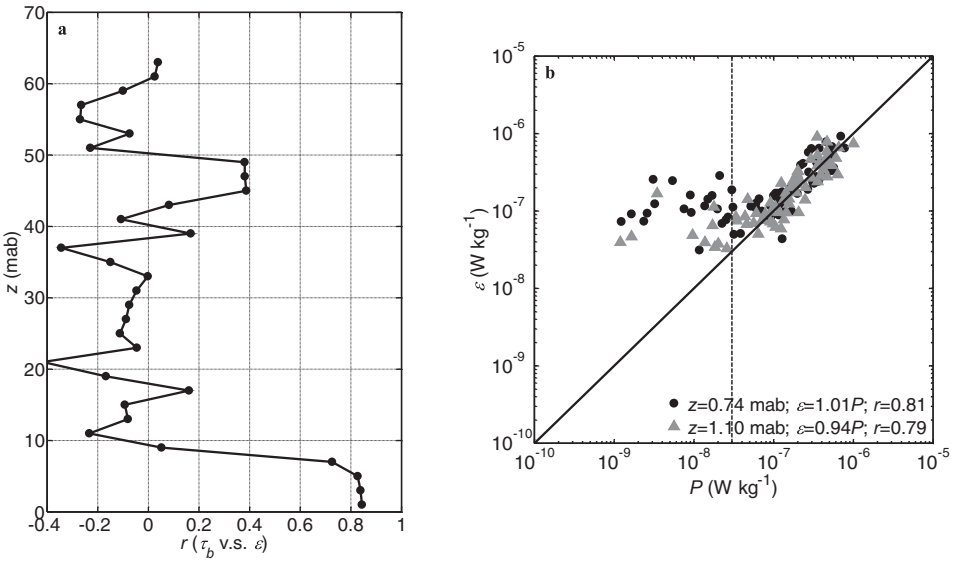

Figure 14. (a) Vertical distribution of correlation coefficient between time series of bottom stress (τ_b) and TKE dissipation rate (ε). (b) Scatterplot of TKE production rate (P) versus ε estimated at 0.74 (solid circle) and 1.10 (triangle) mab with straight line indicating the 1:1 ratio.

and S), we get σ=0.33 (Figure 11e). This corresponds to an average difference of 0.33 decades between ε_{MG} and observed ε. The difference can be reduced by slightly modifying the MG model into the form of

$$\varepsilon_{new} = \varepsilon_a \left[\left(\frac{N}{N_0} \right) \left(\frac{S}{S_0} \right) \right]^b, \tag{5}$$

By fitting our data to this new model, we get $\varepsilon_a = 9.2\times10^{-10}$ W kg^{-1} and $b = 0.61$. The new model fit is displayed in Figure 11d. By setting $\varepsilon_{model} = \varepsilon_{new}$ in equation (4), we get σ=0.27 between the observed ε and

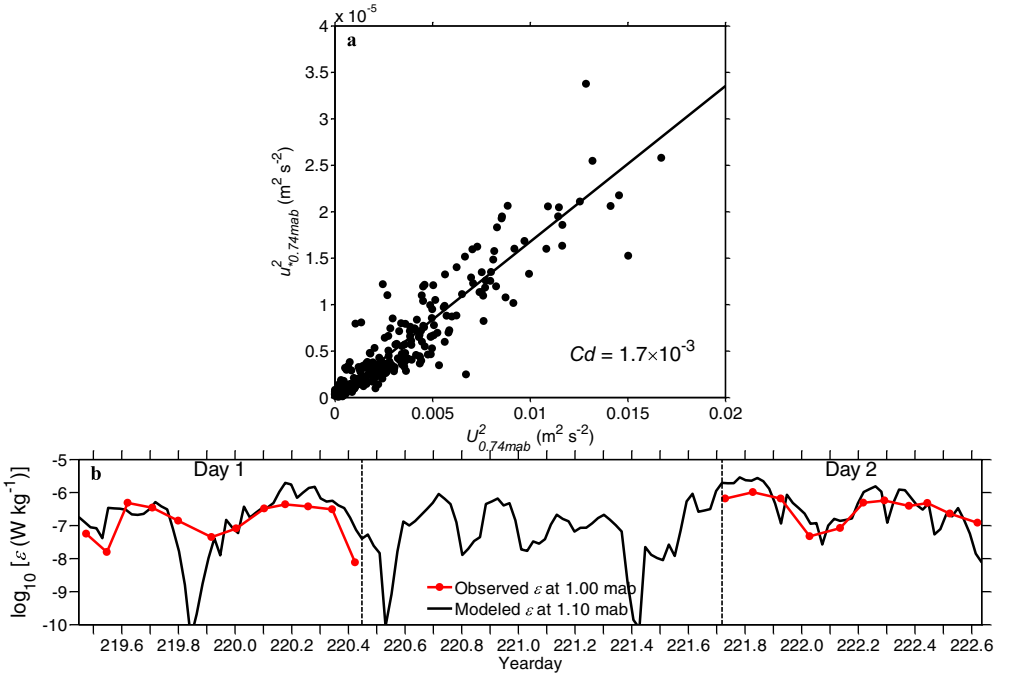

Figure 15. (a) Scatterplot of squared flow speed ($U^2_{0.74mab}$) versus squared friction velocity ($u^2_{*0.74mab}$) at 0.74 mab. The slope of fitted straight line gives $C_D = 1.7\times10^{-3}$. (b) Time series of observed TKE dissipation rate (ε, red) at 1.00 mab and modeled ε according to equation (6) (black) at 1.10 mab.

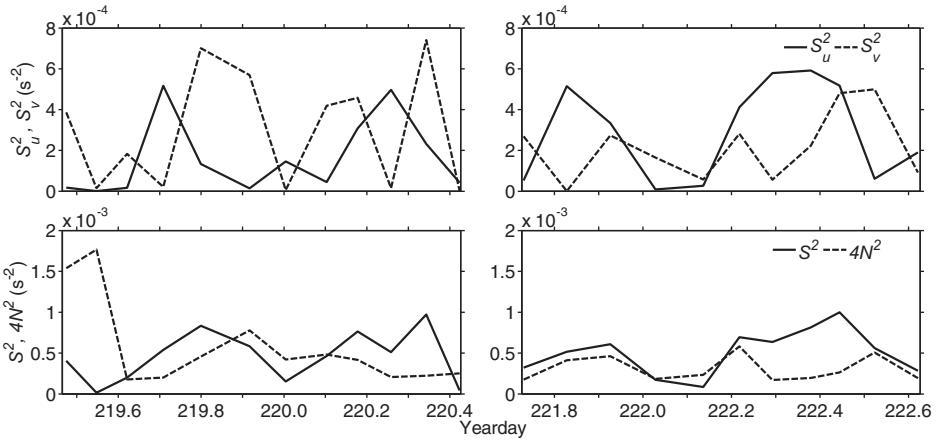

Figure 16. Time series of (top) along-isobath shear variance (S_u^2) and cross-isobath shear variance (S_v^2); (bottom) shear variance (S^2) and four times of buoyancy frequency squared ($4N^2$) at 0.74 mab. Left and right plots show day 1 and day 2, respectively.

model fitted values ε_{new} (Figure 11f), meaning that the average difference is 0.27 decades. While ε_{new} improves the accuracy of fitting compared with ε_{MG}, the underlying physics of determining ε_a and b are still not understood.

4.3. BBL Turbulence

As discussed in section 4.1, strong turbulence in the BBL corresponds to $Ri<0.25$ caused by large shear. Time variations of bottom stress (τ_b, Figure 5c), U (Figure 6c), S^2, Ri, TKE production rate (P) and ε (Figure 8) followed one another. These quantities all show large values during yearday 219.6–219.8 and 220.0–220.4 on day 1 and yearday 221.7–222.0 and 222.2–222.6 on day 2. Figure 14a shows the correlation coefficient between time series of ε at each level and τ_b. The correlation coefficient is large ($r\sim0.8$–0.9) near the bottom and decreases dramatically above 7 mab. This suggests the strong link between BBL turbulence and bottom stress. Figure 14b shows scatterplot of P versus ε at the lowest two levels of BASS. Linear regressions of $\varepsilon = 1.01P$ at 0.74 mab ($r=0.81$) and $\varepsilon = 0.94P$ at 1.10 mab ($r=0.79$) are obtained through least-squares fitting for P larger than 2×10^{-8} W kg^{-1}. The correlation diminishes for P less than 2×10^{-8} W kg^{-1} possibly due to uncertainties in the estimated quantities. Uncertainty in estimating P is primarily associated with that in

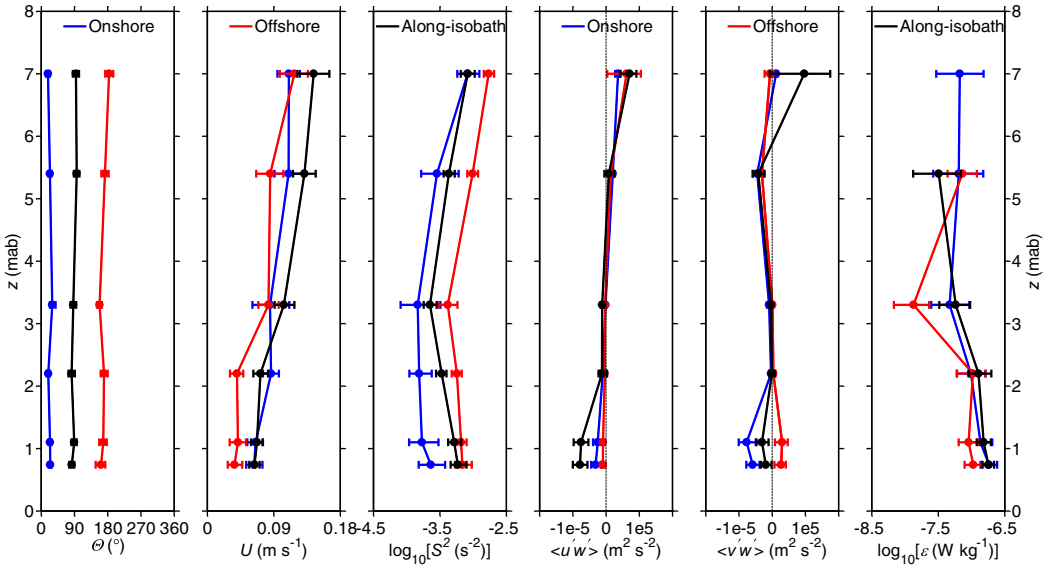

Figure 17. (left to right) Vertical distributions of flow direction (Θ); flow speed (U); shear variance (S^2); along-isobath Reynolds stress ($<u'w'>$); cross-isobath Reynolds stress ($<v'w'>$); and TKE dissipation rate (ε) averaged over onshore (blue), offshore (red) and along-isobath (black) ensembles, respectively. The 95% confidence intervals are shown by horizontal bars.

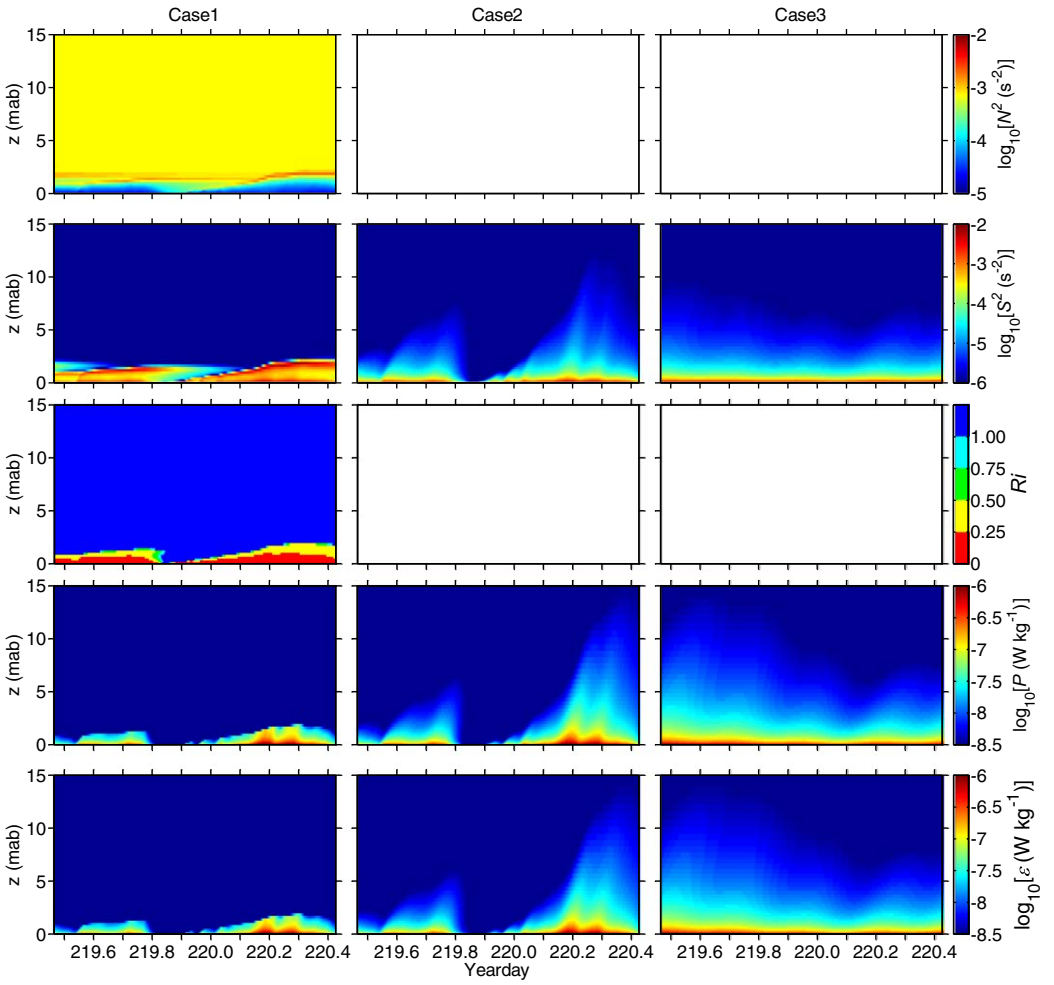

Figure 18. Time-depth variations of (top to bottom) squared buoyance frequency (N^2); shear variance (S^2); gradient Richardson number (Ri); TKE production rate (P) and dissipation rate (ε) simulated by the GOTM on day 1. (left to right) Results for Cases 1, 2, and 3.

estimating Reynolds stress [*Shaw et al.*, 2001]. Such uncertainty leads to many unrealistic estimates of P in the upper four levels of BASS (negative values shown by blank areas in Figures 8k–8l). Further we examine the scaling of ε in the BBL using the law-of-the-wall [*Taylor*, 1920; *Richards et al.*, 2013]:

$$\varepsilon = \frac{C_D^{3/2} U^3}{\kappa z}, \tag{6}$$

where C_D is the bottom drag coefficient and κ=0.4 is the von Karman constant. $C_D = u*^2/U^2$ is obtained using U and friction velocity $\left(u_* = \left[\sqrt{<u'w'>^2 + <v'w'>^2}\right]^{1/2}\right)$ at the lowest level (0.74 mab) of BASS. Figure 15a shows scatterplot of U^2 versus $u2$ * at 0.74 mab; a linear fitting gives $C_D = 1.7\times10^{-3}$. Figure 15b compares the observed ε at 1.00 mab with the predicted ε at 1.10 mab using U at that level and C_D according to equation (6). The good agreement strongly supports that the BBL turbulence in this study is mainly driven by bottom stress. The generation of BBL turbulence by internal waves cannot be a dominant factor, because of the negative correlation between N^2 and ε (Figure 10b). The energy of internal waves (hence the wave-generated turbulence) increases with increasing N according to theory [*Gill*, 1982].

Figures 6 and 8 have shown that U, S^2, Ri and ε in the BBL all have two broad peaks in 1 day, in contrast to the presence of four peaks in 1 day in many sites controlled by M_2 barotropic tide [e.g., *Simpson et al.*, 1996]. Figure 16 shows the time series of S^2 and N^2 at the lowest level of BASS (0.74 mab). The along and cross-isobath components of shear variance, S_u^2 and S_v^2, both contribute to variation of the total shear

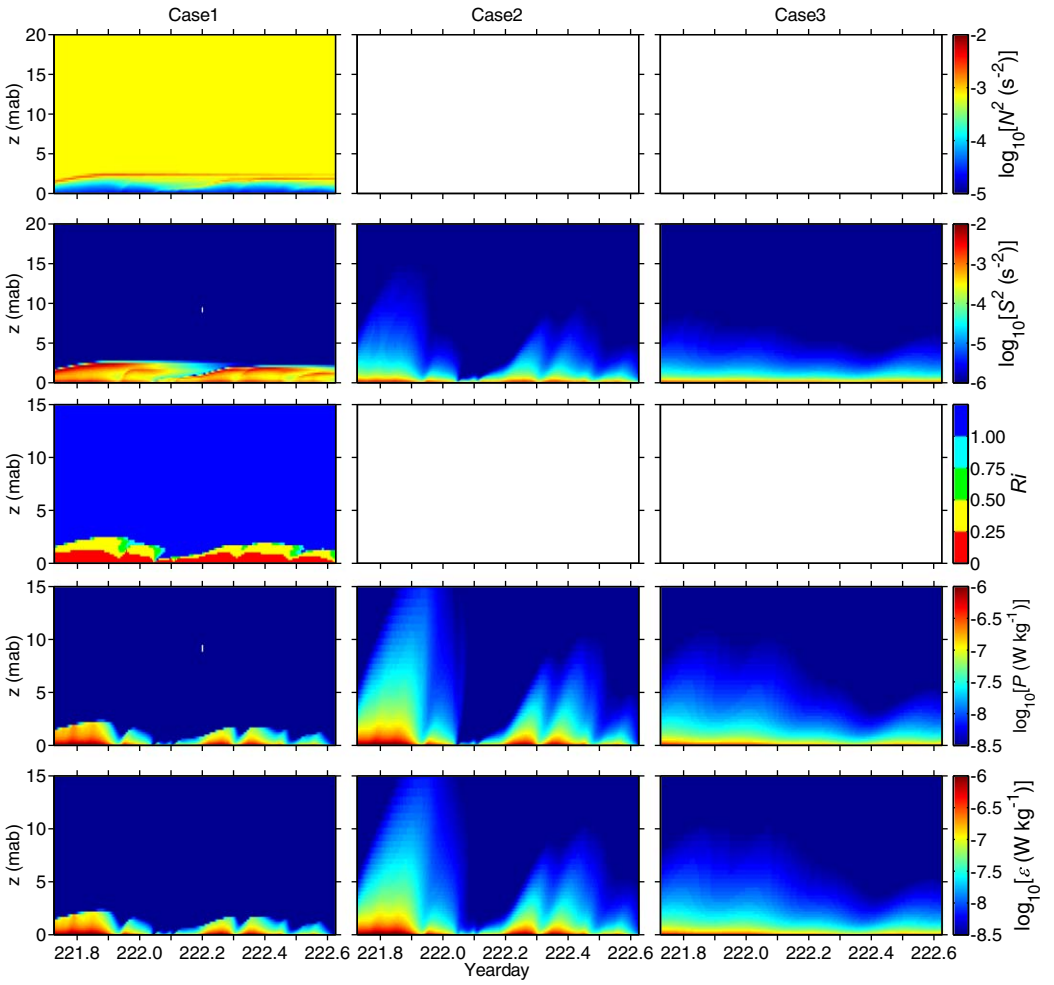

Figure 19. Same as Figure 18 but for day 2.

variance S^2. The along and cross-isobath components of shear combined to cause ε to have two peaks in 1 day. This behavior is related to the presence of a subtidal flow in addition to the oscillating tidal flow at the study site, to be demonstrated by model simulations at the end of this section.

The time variation of BBL turbulence is related to changes in shear and stratification, associated with flow direction Θ (Θ=0° at 0°T). The boundary layer variables are separated into three groups, an eastward along-isobath flow group with $\Theta>=50°$ and $\Theta<=130°$, an onshore flow group with $\Theta>=-40°$ and $\Theta<=40°$, an offshore flow group with $\Theta>=140°$ and $\Theta<=220°$. Vertical distributions of Θ, U, S^2, along-isobath Reynolds stress ($<u'w'>$), cross-isobath Reynolds stress ($<v'w'>$) and ε averaged over onshore, offshore and along-isobath ensembles, respectively, are shown in Figure 17. At the lowest two levels (0.74 and 1.10 mab), magnitudes of $<u'w'>$ during along-isobath flow and $<v'w'>$ during cross-shore flow are large due to bottom friction, and ε reaches maximum. At the third and fourth layers (2.20 and 3.30 mab), Reynolds stresses decrease to near zero corresponding to minimal shear, and ε is small. Above 4 mab, $<u'w'>$, $<v'w'>$, and S^2 increase, but ε remains small. Figures 8k–8l suggests an increase of TKE production above 4 mab, hence the small ε must be due to the loss of TKE to buoyancy. One interesting phenomena is that stronger shear during offshore flow does not lead to larger dissipation rate; instead, weaker shear during onshore flow produces larger dissipation rate. This may be related to the presence of cross-isobath density gradient. During onshore flow, the decrease of the flow speed toward the bed results in differential transport of water masses, saltier water is moved above fresher water in the BBL, potentially leading to unstable stratification and convective mixing, similar as the process of shear-induced convection discussed by *Lorke*

et al. [2005]. During offshore flow, the same differential transport mechanism as described above moves fresher water on top of saltier water. This leads to stronger stratification in the BBL on the slope.

The coexistence of tidal and subtidal flows as well as the cross-shelf density gradient determines the depth-time variations of turbulence and mixing in the BBL and the layer immediately above at the study site. The eastward subtidal current leads to onshore Ekman transport and, hence, the creation of the lower stratified layer, which inhibits the upward extension of BBL turbulence. Otherwise, turbulence produced in the BBL would extend further into the interior, or at least the height of BBL would not be limited by stratification. The relevance of these mechanisms to the observed characteristics is illustrated with simulations using an idealized model. The model is introduced in the Appendix A. Figures 18 and 19 show the time-depth variations of N^2, S^2, Ri, P and ε at 0–15 mab on day 1 and day 2, respectively, from three simulations. Case 1 includes tidal and subtidal flows and the influence of stratification. The model solution shows common characteristics with observations: larger values of S^2 are confined near the bottom and lead to $Ri<0.25$; P and ε in the BBL have two peaks in 1 day; outside the BBL, weak shear and stratification lead to $Ri>1$ and small values of P and ε. Case 2 retains subtidal flow but excludes stratification. It still obtains two peaks of P and ε in 1 day, but results in bottom-generated turbulence that extends upward to the water column with an evident phase lag. Case 3 excludes the influences of subtidal flow and stratification. It obtains four peaks of P and ε on 1 day; lower upward extension of shear, P and ε compared with Case 2, especially on day 2.

5. Conclusions

The Coastal Mixing and Optics experiment obtained a comprehensive data set to study mixing in shelf waters. In this study, through analyzing 2 days of observations in summer of 1997, a representation of layered stratification and turbulent mixing is further revealed. A novel aspect of the present study is the addition of BBL measurements to the well-analyzed midcolumn observations. Starting from 5 m below the surface, the water column can be divided into four layers according to N^2: the subsurface stratification layer; the middepth weak stratification layer; the lower stratification layer and the well-mixed BBL.

An important physical process in our observation is the eastward subtidal current, which served to control the hydrography and mixing characteristics. The eastward subtidal current led to bottom Ekman onshore transport, which resulted in stronger onshore than offshore flow. The combination of onshore flow with local eastward subtidal current changed the magnitude and periodic variation of BBL mixing.

Another important factor influencing the hydrography and mixing features is the shelf slope topography. The density gradient across the slope and the onshore bottom Ekman flow contributed to the presence of a lower stratified layer. In the BBL, the density gradient and the differential transport favors the creation of convective mixing during onshore flow and rather strong stratification during offshore flow.

The existence of a lower stratified layer inhibited the upward extension of the strong turbulence in the BBL. Mixing in the BBL under a shear instability condition was mainly caused by bottom stress, whereas that in midcolumn under stable conditions was mainly related to near-inertial and semidiurnal internal waves. Positive correlations between N^2 and S^2, S^2 and ε, N^2 and ε are found in midcolumn water but not in the BBL. Midcolumn ε showed no dependence on Ri, but increased with increasing N and S. We note that the estimates of N, S and Ri here are based on fine-scale measurements.

The MG model reasonably describes the dependence of the observed ε in the interior water column on N and S. However the scatter of the parameter ε_0 for different data sets limits the general applicability of the model. Based on three different data sets from the same site on the New England Shelf, we conclude that (1) similar ranges of N^2 lead to similar ε_0 for MG model; (2) ε_0 decreases with increasing N^2; and (3) the relationship of ε_0 versus N^2 may be determined by local bathymetric parameters.

Appendix A: Modeling BBL Turbulence With the General Ocean Turbulent Model (GOTM)

A Cartesian coordinate system is defined with the x and y axes pointing to the along and cross-isobath directions shown in Figure 1, and the z axis directed normal to the bottom slope and positive in upward direction. The following assumptions are made: zero mean flow in z direction; hydrostatic approximation in

Table A1. Basic Parameters of the GOTM Model

Parameters	Values	Parameters	Values
c_1	1.44	σ_k	1.00
c_2	1.92	σ_ε	1.30
c_3^-	−0.62	c_μ^0	0.5562
c_3^+	1.00	κ	0.40

the z momentum equation; zero advection in the x and y momentum equations; zero turbulent mixing in x and y directions. The governing equations of the model are written as:

$$\frac{\partial u}{\partial t}=-\frac{1}{\rho_0}\frac{\partial p}{\partial x}+fv+\frac{\partial}{\partial z}\left(v_t\frac{\partial u}{\partial z}\right), \tag{A1}$$

$$\frac{\partial v}{\partial t}=-\frac{1}{\rho_0}\frac{\partial p}{\partial y}-fu+\frac{\partial}{\partial z}\left(v_t\frac{\partial v}{\partial z}\right), \tag{A2}$$

$$\frac{\partial p}{\partial z}=-\rho g, \tag{A3}$$

$$\frac{\partial b}{\partial t}=\frac{\partial}{\partial z}\left(v_t^b\frac{\partial b}{\partial z}\right), \tag{A4}$$

where u and v are along and cross-isobath velocities; p is pressure; f is the Coriolis parameter; $b=-g(\rho-\rho_0)/\rho_0$ is buoyancy; ρ is density and ρ_0 its reference value; g is the acceleration due to gravity; v_t and v_t^b are the vertical eddy viscosity and diffusivity, respectively. The surface boundary conditions are

$$b=0, p=0, \rho_0 v_t\frac{\partial u}{\partial z}=0, \rho_0 v_t\frac{\partial v}{\partial z}=0, \text{at } z=H, \tag{A5}$$

where H is water depth. The bottom boundary conditions are

$$u=0, v=0, \frac{\partial b}{\partial z}=0, \text{ at } z=0. \tag{A6}$$

A second-order turbulent closure model [*Umlauf and Burchard*, 2005] is solved to compute v_t and v_t^b according to

$$v_t=c_\mu\frac{k^2}{\varepsilon}; v_t^b=c_\mu^b\frac{k^2}{\varepsilon}, \tag{A7}$$

where c_μ and c_μ^b are stability functions. The density (k) and dissipation rate (ε) of turbulent kinetic energy (TKE) are calculated by solving

$$\frac{\partial k}{\partial t}-\frac{\partial}{\partial z}\left(\frac{v_t}{\sigma_k}\frac{\partial k}{\partial z}\right)=P+B-\varepsilon, \tag{A8}$$

$$\frac{\partial \varepsilon}{\partial t}-\frac{\partial}{\partial z}\left(\frac{v_t}{\sigma_\varepsilon}\frac{\partial \varepsilon}{\partial z}\right)=\frac{\varepsilon}{k}(c_1P+c_3B-c_2\varepsilon), \tag{A9}$$

where $P=v_t\left(\frac{\partial u}{\partial z}\right)^2$ is the TKE production rate; $B=\frac{\partial}{\partial z}\left(v_t^b\frac{\partial b}{\partial z}\right)$ is rate of TKE loss to the buoyancy; σ_k, σ_ε, c_1, c_2, and c_3 are basic model parameters (Table A1). The boundary conditions for k and ε are

$$v_t\frac{\partial k}{\partial z}=0 \text{ at } z=H \text{ and } z=0, \tag{A10}$$

$$\frac{v_t}{\sigma_\varepsilon}\frac{\partial \varepsilon}{\partial \tilde{z}}=-\left(c_\mu^0\right)^3\frac{v_t}{\sigma_\varepsilon}\frac{k^{3/2}}{\kappa(\tilde{z}+z_0(z_0^s,\ z_0^b))^2}, \tag{A11}$$

where κ is von Karman constant; c_μ^0 is another basic model parameter (Table A1); z_0 is the roughness length at surface (z_0^s) or bottom (z_0^b) (Table A2); and $\tilde{z}$ is the distance from the bottom or surface. Details of model numerical implementation are provided in *Burchard et al.* [2005].

Table A2. Specific Parameters of the GOTM Model for Cases 1–3

	Forcing Velocity	Initial N^2	Other Parameters
Case 1	Velocity at 0.74 mab from BASS	7×10^{-4} s^{-2}	H=70 m
Case 2	Velocity at 0.74 mab from BASS	0	$z_0^s=0.02$ m
Case 3	Barotropic tidal velocity from OTIS	0	$z_0^b=4.5\times10^{-5}$ m $f=9.47\times10^{-5}$ s^{-1}

Table A2 lists the specific model parameters used for the BBL simulation and Cases 1–3. The setting of surface pressure as zero does not mean that the model has no external forcing. The forcing is introduced by specifying the velocity at a certain height or vertical mean

velocity with the observed time series. This effectively introduces a barotopic pressure gradient [*Burchard*, 1999]. In Cases 1 and 2, forcing is introduced using the observed current at 0.74 mab from BASS; in Case 3, forcing is introduced using the barotropic tidal current from OTIS. In Case 1, the initial density distribution are set horizontally uniform with a constant vertical gradient given by $N^2=7\times10^{-4}\ s^{-2}$; in Case 2 and 3, initial $N^2=0\ s^{-2}$. The depth H is set to 70 m. The bottom roughness length z_0^b is estimated according to $z_0^b=ze^{-\frac{\kappa U}{u_*}}$ (derived from the logarithmic velocity profile) using the observed values of U and $u*$ at 0.74 mab. The Coriolis parameter f is set corresponding to the latitude of measurement site.

Acknowledgments

This study was conducted during Jianing Wang's visit to Bedford Institute of Oceanography (Canada), which was financially supported by the China Scholarship Council. The field component of this program was jointly supported by the US Office of Naval Research (grants N00014-95-1-1030, N00014-95-1-0373, and N00014-96-1-0953) and Fisheries and Oceans of Canada. The crew of the R/V Oceanus is thanked for their assistance with the collection of the field data. In accordance with the Fisheries and Oceans Canada Policy for Scientific Data (http://www.dfo-mpo.gc.ca/science/data-donnees/policy-politique-eng.htm), all data utilized in this paper are publicly available and can be obtained by contacting the Ocean Data and Information Section (XMAR.ODIS@dfo-mpo.gc.ca) at the Bedford Institute of Oceanography. We thank three anonymous reviewers for thorough and constructive review of the original manuscript.

References

Beardsley, R. C., D. C. Chapman, K. H. Brink, S. R. Ramp, and R. Schlitz (1985), The Nantucket Shoals Flux Experiment (NSFE79), I, A basic description of the current and temperature variability, *J. Phys. Oceanogr.*, *15*, 713–748.

Boicourt, W. C., and P. W. Hacker (1976), Circulation on the Atlantic continental shelf of the United States, Cape May to Cape Hatteras, in *Memoires de la Societe Royale des Sciences de Liege*, edited by J. C. J. Nihoul, pp. 187–200, Univ. of Liege, Liege, Belgium.

Burchard, H. (1999), Recalculation of surface slopes as forcing for numerical water column models of tidal flow, *Appl. Math. Model.*, *23*, 737–755.

Burchard, H., E. Deleersnijder, and G. Stoyan (2005), Some numerical aspects of turbulence-closure models, in *Marine Turbulence: Theories, Observations and Models*, edited by H. Z. Baumert, J. H. Simpson, and J. Sündermann, pp. 197–206, Cambridge Univ. Press, Cambridge, U. K.

Burchard, H., et al. (2008), Observational and numerical modeling methods for quantifying coastal ocean turbulence and mixing, *Prog. Oceanogr.*, *76*, 399–442.

Canuto, V. M., A. Howard, Y. Cheng, and M. S. Dubovikov (2001), Ocean turbulence. Part I: One-point closure model-Momentum and heat vertical diffusivities, *J. Phys. Oceanogr.*, *31*, 1413–1426.

Carter G. S., M. C. Gregg, and R. C. Lien (2005), Internal waves, solitary-like waves, andmixing on the Monterey Bay shelf, *Cont. Shelf Res.*, *25*, 1499–1520.

Davis, K. A., and S. G. Monismith (2011), The modification of bottom boundary layer turbulence and mixing by internal waves shoaling on a barrier reef, *J. Phys. Oceanogr.*, *41*, 2223–2241.

Egbert G. D., and S. Y. Erofeeva (2002), Efficient inverse modeling of barotropic ocean tides, *J. Atmos. Oceanic Technol.*, *19*, 183–204.

Gill, A. E. (1982), *Atmosphere-Ocean Dynamics, Int. Geophys. Ser.*, vol. 30, 662 pp., Academic, N. Y.

Gregg, M. C. (1989), Scaling turbulent dissipation in the thermocline, *J. Geophys. Res.*, *94*, 9686–9698.

Henyey, F. S., J. Wright, and S. M. Flatte (1986), Energy and action flow through the internal wave field: An eikonal approach, *J. Geophys. Res.*, *91*, 8487–8495.

Houghton, R. W., F. Aikman III, and H. W. Ou (1988), Shelf-slope frontal structure and cross-shelf exchange at the New England shelf-break, *Cont. Shelf Res.*, *8*, 687–710.

Howard, L. N. (1961), Note on a paper of John W. Miles. *J. Fluid Mech.*, *10*, 509–512.

Inall, M. E., T. P. Rippeth, and T. J. Sherwin (2000), The impact of non-linear waves on the dissipation of internal tidal energy at a shelf break, *J. Geophys. Res.*, *105*, 8687–8705.

Kunze, E., and S. G. L. Smith (2004), The role of small-scale topography in turbulent mixing of the global ocean, *Oceanography*, *17*, 55–64.

Ledwell, J. R., T. F. Duda, M. A. Sundermeyer, and H. E. Seim (2004), Mixing in a coastal environment: 1. A view from dye dispersion, *J. Geophys. Res.*, *109*, C10013, doi:10.1029/2003JC002194.

Lentz, S. (2010), The mean along-isobath heat and salt balances over the Middle Atlantic Bight Continental Shelf, *J. Phys. Oceanogr.*, *40*, 934–948.

Lentz, S., K. Shearman, S. Anderson, A. Plueddemann, and J. Edson (2003), Evolution of stratification over the New England shelf during the Coastal Mixing and Optics study, August 1996-June 1997, *J. Geophys. Res.*, *108*(C1), 3008, doi:10.1029/2001JC001121.

Liu, Z. (2010), Instability of baroclinic tidal flow in a stratified fjord, *J. Phys. Oceanogr.*, *40*(1), 139–154.

Liu, Z., H. Wei, I. D. Lozovatsky, and H. J. S. Fernando (2009), Late summer stratification, internal waves, and turbulence in the Yellow Sea, *J. Mar. Syst.*, *77*, 459–472.

Lorke, A., F. Peeters, and A. Wüest (2005), Shear-induced convective mixing in bottom boundary layers on slope, *Limnol. Oceanogr.*, *50*, 1612–1619.

MacKinnon, J. A., and M. C. Gregg (2003a), Shear and baroclinic energy flux on the summer New England Shelf, *J. Phys. Oceanogr.*, *33*, 1462–1475.

MacKinnon, J. A., and M. C. Gregg (2003b), Mixing on the late-summer New England Shelf-solibores, shear and stratification, *J. Phys. Oceanogr.*, *33*, 1476–1492.

MacKinnon, J. A., and M. C. Gregg (2005a), Near-inertial waves on the New England Shelf: The role of evolving stratification, turbulent dissipation, and bottom drag, *J. Phys. Oceanogr.*, *35*, 2408–2424.

MacKinnon, J. A., and M. C. Gregg (2005b), Spring mixing: Turbulence and internal waves during restratification on the New England Shelf, *J. Phys. Oceanogr.*, *35*, 2425–2443.

McDougall, T. J. (1987), Neutral surfaces, *J. Phys. Oceanogr.*, *17*, 1950–1964.

Mellor, G. L., and T. Yamada (1974), A hierarchy of turbulence closure models for planetary boundary layers, *J. Atmos. Sci.*, *31*, 1791–1806.

Mellor, G. L., and T. Yamada (1982), Development of a turbulence closure model for geophysical fluid problems, *Rev. Geophys.*, *20*, 851–875.

Miles, J. W. (1961), On the stability of heterogeneous shear flows, *J. Fluid Mech.*, *10*, 496–508.

Oakey, N. S. (1988), EPSONDE: An instrument to measure turbulence in the deep ocean, *IEEE J. Oceanic Eng.*, *13*, 124–128.

Oakey, N. S., and B. J. W. Greenan (2004), Mixing in a coastal environment: 2. A view from microstructure measurements, *J. Geophys. Res.*, *109*, C10014, doi:10.1029/2003JC002193.

Palmer, M. R., T. P. Rippeth, and J. H.Simpson (2008), An investigation of internal mixing in a seasonally stratified shelf sea, *J. Geophys. Res.*, *113*, C12005, doi:10.1029/2007JC004531.

Palmer, M. R., J. A. Polton, M. E. Inall, T. P. Rippeth, J. Green, J. Sharples, and J. H. Simpson (2013), Variable behavior in pycnocline mixing over shelf seas, *Geophys. Res. Lett.*, *40*, 161–166, doi:10.1029/2012GL054638.

Richards, C., D. Bourgault, P. S. Galbraith, A. Hay, and D. E. Kelley (2013), Measurements of shoaling internal waves and turbulence in an estuary, *J. Geophys. Res.*, *118*, 273–286, doi:10.1029/2012JC008154.
Rippeth, T. P. (2005), Mixing in seasonally stratified shelf seas: A shifting paradigm, *Philos. Trans. R. Soc. A*, *363*, 2837–2854.
Rippeth, T. P., J. H. Simpson, R. Player, and M. Garcia (2002), Current oscillations in the diurnal-inertial band in the Catalonian shelf in spring, *Cont. Shelf Res.*, *22*, 247–265.
Rippeth, T. P., J. H. Simpson and E.Williams (2003), Measurement of the rates of production and dissipation of turbulent kinetic energy in an energetic tidal flow: Red Wharf Bay revisited, *J. Phys. Oceanogr.*, *33*, 1889–1901.
Rippeth, T. P., M. R. Palmer, J. H. Simpson, N. R. Fisher, and J. Sharples (2005), Thermocline mixing in summer stratified continental shelf seas, *Geophys. Res. Lett.*, *32*, L05602, doi:10.1029/2004GL022104.
Rohr, J. J., E. C. Itsweire, K. N. Helland, and C. W. V. Atta (1988), An investigation of the growth of turbulence in a uniform-mean-shear flow, *J. Fluid Mech.*, *187*, 1–33.
Sharples, J., C. M. Moore and E. R.Abraham (2001), Internal tide dissipation, mixing, and vertical nitrate flux at the shelf edge of NE New Zealand, *J. Geophys. Res.*, *106*, 14,069–14,081.
Shaw, W. J., and J. H. Trowbridge (2001), The direct estimation of near-bottom turbulent fluxes in the presence of energetic wave motions, *J. Atmos. Oceanic Technol.*, *18*(9), 1540–1557.
Shaw, W. J., J. H. Trowbridge, and A. J. Williams III (2001), Budgets of turbulent kinetic energy and scalar variance in the continental shelf bottom boundary layer, *J. Geophys. Res.*, *106*, 9551–9564.
Shearman, R. K., and S. J. Lentz (2003), Dynamics of mean and subtidal flow on the New England shelf, *J. Geophys. Res.*, *108*(C8), 3281, doi: 10.1029/2002JC001417.
Shearman, R. K., and S. J. Lentz (2004), Observations of tidal variability on the New England shelf, *J. Geophys. Res.*, *109*, C06010, doi:10.1029/2003JC001972.
Simpson, J. H., and J. R. Hunter (1974), Fronts in the Irish Sea, *Nature*, *250*, 404–406.
Simpson, J. H., and J. P.Tinker (2009), A test of the influence of tidal stream polarity on the structure of turbulent dissipation, *Cont. Shelf Res.*, *29*, 320–332.
Simpson, J. H., W. R. Crawford, T. P. Rippeth, A. R. Cambell, and J. V. S. Cheok (1996), The vertical structure of turbulent dissipation in shelf seas, *J. Phys. Oceanogr.*, *26*, 1579–1590.
Sundermeyer, M. A., and J. R. Ledwell (2001), Lateral dispersion over the continental shelf: Analysis of dye release experiments, *J. Geophys. Res.*, *106*, 9603–9621.
Taylor, G. (1920), Tidal friction in the Irish sea, *Philos. Trans. R. Soc. London A*, *220*, 1–33.
Umlauf, L., and H. Burchard (2005), Second-order turbulence closure models for geophysical boundary layers. A review of recent work, *Cont. Shelf Res.*, *25*, 795–827.
van der Lee, E. M., and L. Umlauf (2011), Internal wave mixing in the Baltic Sea: Near-inertial waves in the absence of tides, *J. Geophys. Res.*, *116*, C10016, doi:10.1029/2011JC007072.
van Haren, H., L. Mass, J. T. F. Zimmerman, H. Ridderinkhof, and H. Malschaert (1999), Strong inertial currents and marginal internal wave stability in the central North Sea, *Geophys. Res. Lett.*, *26*, 2993–2996.
Wright, W. R. (1976), The limits of shelf water south of Cape Cod, 1941 to 1972, *J. Mar. Res.*, *34*, 1–14.